# THREE-DIMENSIONAL AND MULTI-TEMPORAL DUNE-FIELD PATTERN

# ANALYSIS IN THE OLYMPIA UNDAE DUNE FIELD, MARS

A Thesis

by

WILLIAM DAVID MIDDLEBROOK

Submitted to the Office of Graduate and Professional Studies of
Texas A&M University
in partial fulfillment of the requirements for the degree of

MASTER OF SCIENCE

| | |
|---|---|
| Chair of Committee, | Ryan Ewing |
| Committee Members, | Michael Bishop |
| | Chris Houser |
| Head of Department, | Rick Giardino |

August 2015

Major Subject: Geology

# ABSTRACT

Fields of sand dunes are ubiquitous in the north polar region of Mars and provide a record of sand transport processes influenced by Mars' polar climate. Spatial and temporal variations in dunes, ripples, coarse-grained ripples, and exposed dune cross-strata were analyzed in two areas of the Olympia Undae Dune Field in order to assess the influence of the Martian polar boundary conditions on ripple and dune activity and on pattern development. Two- and three-dimensional parameters, including dune crest length, spacing, width, slope, and height, were statistically assessed using regression analysis and descriptive statistics. Sediment fluxes were calculated using Co-registration of Optically Sensed Imagery and Correlation (COSI-Corr), a program that precisely co-registers and correlates imagery, and by measuring dune displacement.

Two-dimensional pattern analysis indicates the co-existence of two populations of dunes that can be interpreted as two generations or as forming simultaneously under sediment availability limited conditions. Three-dimensional pattern analysis shows an asymmetry in slope profiles of the primary dunes and is consistent with primary dunes forming transversely to constructional winds. Four different types of ripple crestline patterns are identified and likely arise due to differences in grain size and dune-modified wind speeds and secondary flow directions. Maximum measured ripple displacement in the center of Olympia Undae study area is ~1.4 m yr$^{-1}$ ± 0.13 m. Assuming a mean ripple height of 0.11 m and a 4:1 saltation to reptation ratio, the sediment flux is ~0.42 m$^3$ m$^{-1}$ yr$^{-1}$.

Adjacent to the polar ice cap, barchan dune crest displacements range between 0.25 m yr$^{-1}$ and 2.80 m yr$^{-1}$ and dune heights between 11 m and 31 m. Mean sediment flux is 3.5 m$^3$ m$^{-1}$ yr$^{-1}$. Results indicate that there is a spatial decay in sediment transport across the field and that fluxes near the cap are comparable to those found in Nili Patera, Mars and Victoria Valley, Antarctica. Overall the polar boundary conditions seasonally limit sand availability by seasonal frost cover and subsurface ice. The polar boundary conditions are most influential at the dune pattern scale, but appear to have little influence on the ripple pattern or ripple mobility.

# ACKNOWLEDGEMENTS

TABLE OF CONTENTS

LIST OF FIGURES

viii

LIST OF TABLES

# 1. INTRODUCTION

Fields of sand dunes are widespread across the surface of Mars. These dune fields form a rich array of patterns that reflect the internal dynamics of dune-field pattern self-organization and the geomorphic and climatic boundary conditions within which the patterns developed (Ewing et al., 2010, Kocurek et al., 2010). Planetary-scale boundary conditions, such as lower gravity (i.e., 3.71 m/s$^2$) and lower atmospheric density (i.e., 6.0 millibar), have not been shown to significantly influence dune-field pattern formation on Mars (i.e., dune patterns on Mars and Earth are similar at the pattern-scale) (Kocurek and Ewing, 2012). However, the influence of spatially (i.e., latitudinally) and temporally (i.e., seasonally) varying Martian boundary conditions on dune-field pattern formation remains relatively unexplored.

The north polar region of Mars experiences strong seasonal boundary conditions and contains large, spatially varying dune field patterns (Tsoar, 1983; Ewing et al., 2010; Horgan and Bell, 2012). This region is well suited to study how dune field patterns evolve under Martian polar boundary conditions because the seasonal volatile ice cap and the topography of Planum Boreum strongly influence the timing and intensity wind patterns (Smith et al., 2015). Additionally, the north polar dunes are recognized to be active, which affords not only the opportunity to assess the static dune-field pattern, but also the dynamics of dunes and ripples under seasonally changing boundary conditions (Bourke et al, 2008; Hansen et al., 2011, Horgan and Bell, 2012).

The purpose of this study is to assess the boundary conditions in the Olympia Undae Dune Field, which flanks Mars' north polar ice cap, and determine how polar boundary conditions influence dune-field pattern formation and sediment transport on Mars. We analyze spatial variations in dunes, ripples, coarse-grained ripples, and polygonally fractured interdune areas and temporal variations in dunes and ripples. The primary conclusions of this paper are that (1) the seasonal volatile cap and the topography of Planum Boreum are the overarching boundary conditions that dictate much of the pattern in Olympia Undae, (2) sediment availability, as inferred by exposed interdune area, varies spatially in Olympia and may account for changes in pattern organization, (3) three-dimensional dune pattern statistics indicate that the pattern is emerging under an oblique wind regime with winds likely from polar easterlies and katabatic winds, (4) distinct ripple types occur and reflect the boundary condition control of the dune topography, and (5) sand fluxes adjacent to Planum Boreum are significantly greater (up to seven times greater) than those in the interior of Olympia Undae.

# 2. MARS POLAR BOUNDARY CONDITIONS

Boundary conditions are external environmental variables that control the evolution of dune field patterns over time (Werner, 1999; Ewing and Kocurek, 2010). In the north polar area of Mars, a multi-modal wind regime, seasonally-limited sediment availability, preexisting dune topography, grain size, modern and ancient sediment sourcing, the geometry and elevation of Olympia Planum, and its proximity to the perennial polar ice cap, are the boundary conditions that give rise to Olympia Undae Dune Field pattern.

## 2.1 Mars' North Polar Wind Regime

Observation of dune and ripple orientations and atmospheric modeling indicate that the north polar wind regime is comprised of circumpolar easterly winds and a NE wind that is thought to be related to katabatics descending from Planum Boreum (Tsoar et al., 1979; Howard, 2000; Tanaka and Hayward, 2008; Spiga and Forget, 2009; Ewing et al., 2010; Smith et al., 2013). Circumpolar easterly winds are likely the dominant wind mode and are transverse to the primary dune pattern (Ewing et al., 2010). Katabatic winds arise because of the contrast in elevation and albedo of the ice and sediment between Planum Boreum and the lower lying areas, which results in a pressure gradient that drives dense, cold air flows from the cap into Olympia Undae (Tsoar et al., 1979; Howard, 2000; Smith et al., 2010). Frost streaks show that the katabatic flows converge

into chasmae and reentrants of Planum Boreum, one of which has been identified as the major drainage area into Olympia Undae (Howard, 2000). Channelized katabatics may strongly control the evolution of the scarp, eroding reentrants and supplying sediment to the dune field (Howard, 2000; Tanaka et al., 2008; Massé et al., 2012).

*2.2 Sediment Availability*

Sediment availability can be defined as the potential for surficial sediment to be transported by wind (Kocurek and Lancaster, 1999). Variables that may limit sediment availability include chemical cementation, surface roughness, and sediment properties like grain size and sorting (Kocurek and Lancaster, 1999). In the north polar region, the seasonal frost cover and subsurface ice likely restrict aeolian transport for a significant portion of the year (Bourke et al., 2008).

The seasonal ice cap is comprised of $CO_2$ and $H_2O$ ices, which are deposited from the atmosphere during the Martian winter (Kelley et al., 2006; Calvin et al., 2012). Sublimation occurs during the Martian spring due to the increasing flux of solar radiation (Kelley et al., 2006). Maximum frost thickness is 1.5-2 m and occurs north of 80° latitude (Smith et al., 2001). In the north polar region, there is spatial and yearly variability in volatile deposition, which is hypothesized to be related to local topographic and wind conditions (Appéré et al., 2011; Calvin et al., 2012). In contrast to the south pole, $CO_2$ frost cover completely sublimes during the Martian summer (Kelley et al., 2006).

The north polar dunes are thought to be niveo-aeolian features with a desiccated top layer approximately 6 cm thick and an underlying water-ice layer (Feldman, et al., 2008). This interpretation is supported by evidence for tensional fractures and outgassing sublimation pits (Feldman, et al., 2008; Hansen, et al., 2011). The presence of subsurface ice near the dune surface would act to limit sediment availability by binding the sand with ice. The process of volatile sublimation during the onset of the summer may increase sediment availability by loosening sediment that would otherwise be unavailable for transport or by reducing friction between grains (Hansen et al., 2011). This process has been posited as an explanation for the ubiquity of aeolian transport in the north polar region in comparison to other areas of the planet (Hansen et al., 2011).

Spatial variations in sediment availability in the dune field are recognized by the amount of exposed interdune area, which are bright compared to the dunes in the optical satellite images. Variations in spatial availability occur outward from Planum Boreum and from east to west across the field. High Resolution Imaging Science Experiment imagery shows that in the eastern portion of Olympia Undae, dunes are typically spaced such that the toe of upwind dunes are immediately adjacent to the foot of the downwind dune and interdune areas occur less frequently and are spatially constrained, both of which are indicators of high sediment availability. In contrast, to the west, frosted interdune areas are more common and more spatially extensive, indicating that sediment availability is lower. This spatial variation in sediment availability should drive spatial changes in the dune pattern and can be used to test the hypothesis that seasonal sediment

availability affects dune pattern development and evolution by comparing dune pattern parameters in areas of differing sediment availability.

*2.3 Sediment Sourcing*

The location and geometry of source areas in Olympia Undae Sand Sea are strong controls on spatial variations in dune patterns and grain size. The strongest control on the dune-field pattern directly adjacent to Planum Boreum is the point and line source area geometries that arise from sand ablated from Planum Boreum and transported by katabatic winds into the dune field (Ewing et al., 2010). This creates a pattern in which the dunes grow in spacing and height and decrease in defect density away from the source-area (Ewing and Kocurek, 2010). The general E-W decrease in sediment availability within the main Olympia Undae dune field suggests that a source area may exist at the eastern margin of the dune field, which is consistent with the E-W spatial decrease in gypsum (Langevin et al., 2005).

The cavi unit, which underlies and is exposed at the edge of Planum Boreum, is the primary source of the sand and is separated from the distal dunes in Olympia Undae by hundreds of kilometers (Tanaka et al., 2008). The cavi unit is comprised of cross-bedded sediment and ice (Kocurek and Ewing, 2012). Analysis of strata exposed at the margin of Planum Boreum indicates that the unit was deposited by dunes under aeolian processes (Tanaka et al., 2008; Kocurek and Ewing, 2012). Thus, the sediment in Olympia Undae has been through at least two cycles of aeolian transport and is expected to be comprised primarily of well-rounded and well-sorted sediment and show little

6

spatial heterogeneity across the field.  However, some degree of grain size variability has been inferred from variations in ripple wavelength within the field. Ripple wavelength is known to be closely related to grain size on Earth (Bagnold, 1941; Seppälä and Linde, 1978), thus longer wavelength coarse-grained ripples juxtaposed to smaller wavelength ripples indicate variation in grain size (Ewing, et al., 2010). The areal extent of these ripples is typically constrained to the lower lying interdune areas and at the upwind margins adjacent to Planum Boreum.

*2.4 Dune Topography*

Dune topography can control the development of subsequent dune development (Ewing et al., 2006). In Olympia Undae, the dune pattern has been interpreted as complex, with multiple generations of dune development (Ewing et al., 2010). In this interpretation, the primary dunes are a boundary condition to the emergence of the younger secondary dunes (Ewing et al., 2010).

Dune topography also impacts the emergence and development of ripples. Wind is slaved to the dune topography, thus the interaction between topography and wind controls the orientation of the wind ripple crests. Dune topography similarly controls the speed of secondary winds (Jackson and Hunt, 1975). Flow speed-up occurs up the stoss slope of the primary dune due to airflow compression, while under transverse to oblique wind conditions, flow detachment and a wake develop in the lee of the dune (Frank and Kocurek, 1996a). Additionally, variations in wind speed and direction caused by the dune-topography interaction control grain sorting and give rise to the spatial sorting of

7

coarse-grained ripples within the stoss-slope troughs and adjacent to the interdune areas (Frank and Kocurek, 1996b).

# 3. OLYMPIA UNDAE DUNE FIELD

The Olympia Undae Dune Field is the largest dune field on Mars spanning over 385,000 km and is located in the north polar region of Mars (Hayward et al., 2007). The field sits upon Olympia Planum, an 800-meter high platform rising above the Vastitas Borealis plains and adjacent to the Planum Boreum, the perennial north polar ice cap (Figure 1). The dune field is composed primarily of basaltic grains, with a secondary hydrated mineral component, assumed to be gypsum, which is highest in concentration to the east and decreases to the west (Langevin et al., 2005; Fishbaugh et al., 2007; Zimbelman, et al., 2013).

Crescentic and barchan dunes are the most common dune types in Olympia Undae (Tsoar et al., 1979; Ewing et al., 2010). Crescentic dunes form the interior of the field, whereas barchan dunes frequently occur at the southern and western perimeter. Two prominent dune types form a reticulate pattern comprise the majority of the field: asymmetric primary dunes with distinct stoss and lee slopes and rounded secondary dunes that occur between primary dune crestlines (Ewing et al., 2010).

*3.1 Study Areas*

Study Area 1 is located in the southwestern part of the dune field, near the Jojulta Crater at ~81° latitude and 179° longitude (Figure 1). The area features primary dunes oriented N-S and secondary dunes that intersect the primary dunes NE-SW, which form
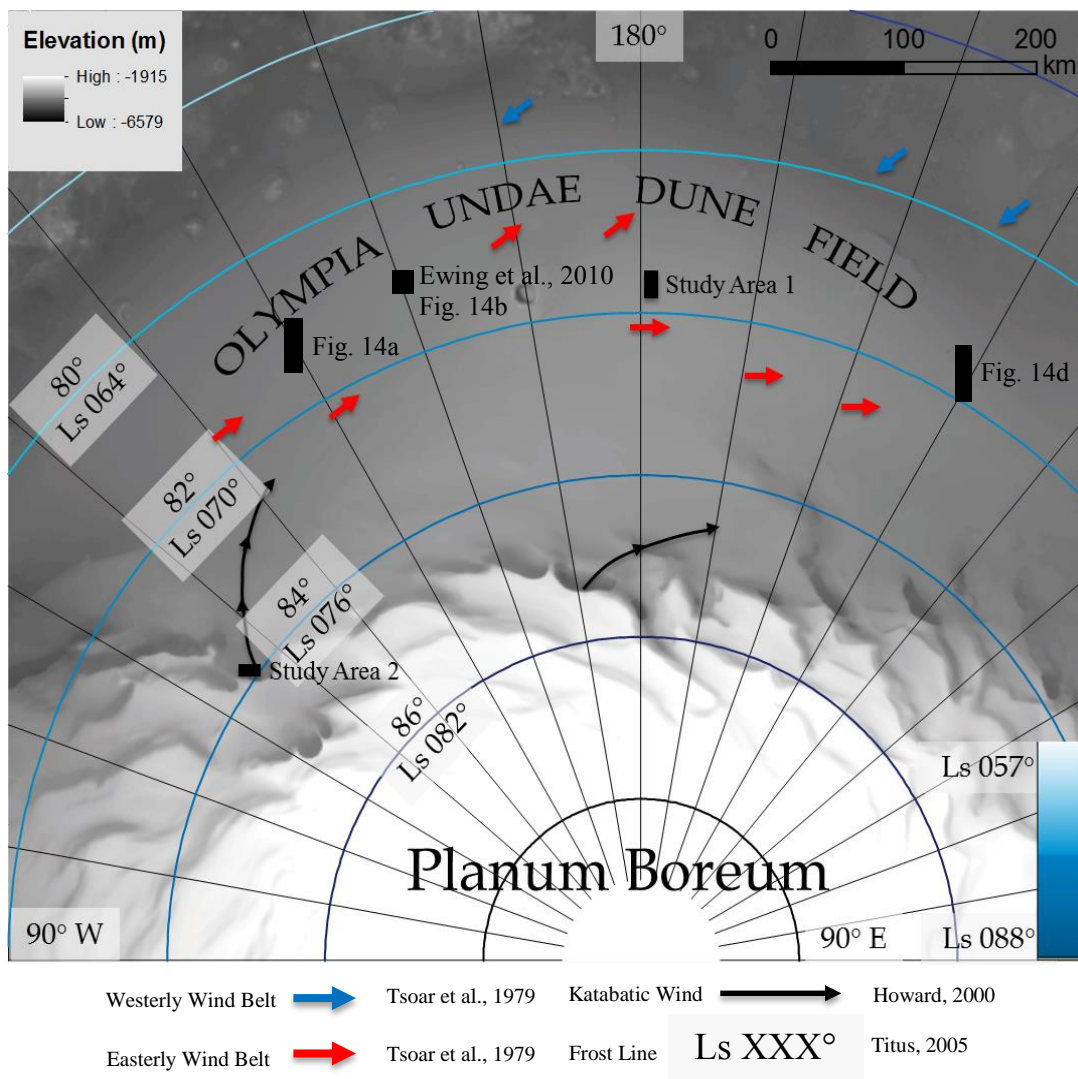
Figure 1. North polar DTM. Study Area 1 is located in Olympia Undae and Study Area 2 is adjacent to the perennial ice cap, Planum Boreum. Circumpolar easterly winds (red arrows) and density driven katabatics (black arrows) comprise the north polar wind regime. Seasonal changes in $CO_2$ frost cover are hypothesized to limit sediment availability for the majority of the year (lines of latitude, extrapolated from Titus, 2005).

an overall reticulate dune-field pattern. The primary dunes are asymmetric, and typically have sharp crestlines, whereas the secondary dunes are rounded and do not show distinct windward and leeward sides (Figure 2). In addition to the larger scale dunes, there are two populations of ripples: coarse-grained ripples and typical aeolian wind ripples. Coarse-grained ripples primarily occur in the interdune areas bordering the polygonal interdune areas and have more widely spaced crests. In contrast, wind ripples typically occur on every sediment-covered surface. Arcuate ridges, which have been interpreted as dune cross-stratification, occur in the interdune areas (Ewing et al., 2010).

Study Area 2 is located adjacent to the Planum Boreum perennial polar ice cap in a cavi reentrant (Figure 1). At the upwind margin of the field, dome dunes, protodunes, and barchans dunes are the predominant dune types that evolve into barchanoid ridges downwind (Figure 3). Two slipface orientations are present in Study Area 1, one parallel to the dominant crestline trend, which is parallel to the local orientation of the escarpment and one perpendicular to dune orientation. As in Study Area 1, wind ripples occur on all sediment covered surfaces, whereas coarse-grained ripples occur at the upwind margin of the field and in the interdune areas.
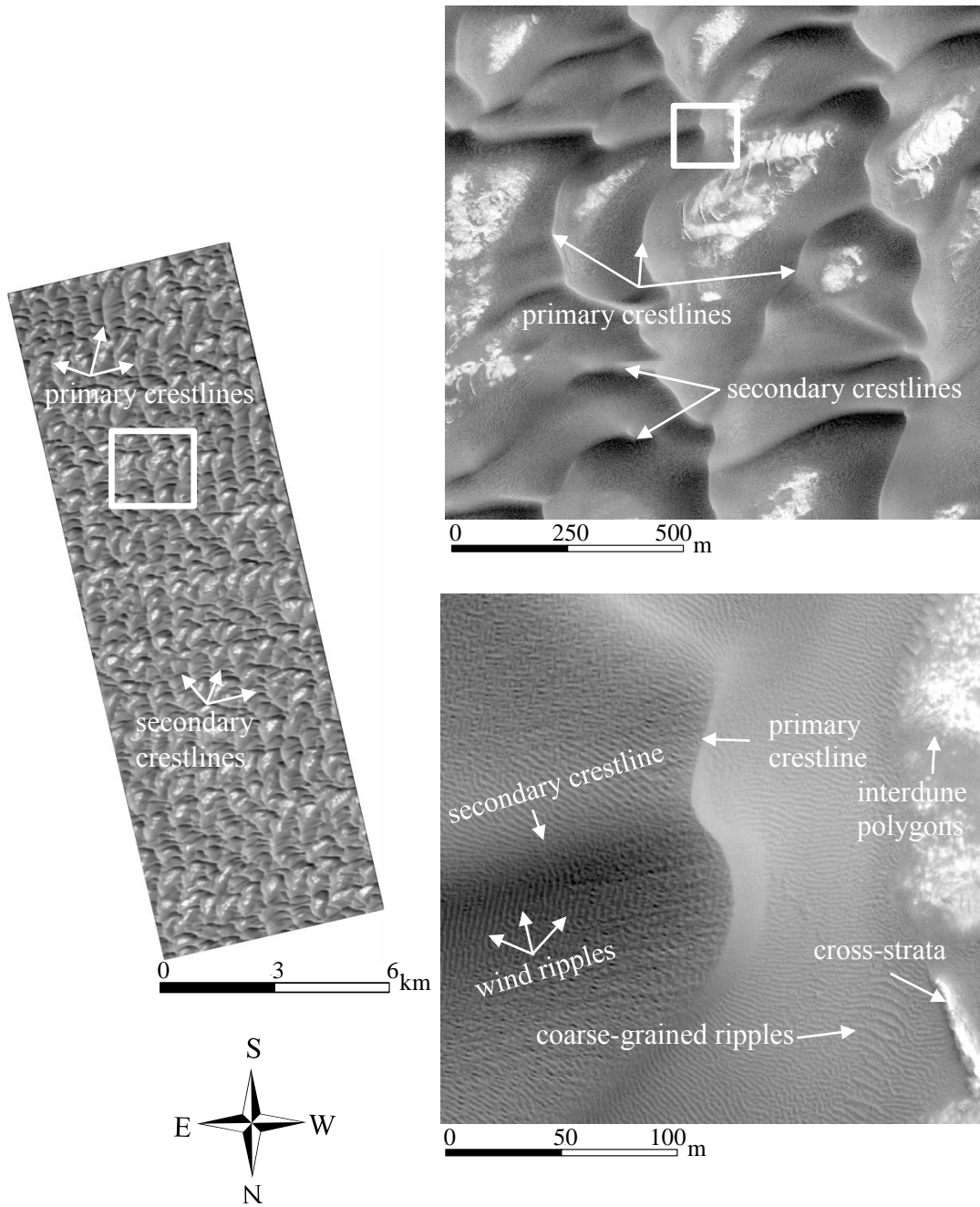
Figure 2. Study Area 1: ESP_027713_2615, Ls 130°, 6-24-2012. (a) HiRISE image of Study Area 1. (b) N-S trending primary dunes and the E-W trending secondary dunes. (c) Wind ripples, coarse-grained ripples, dune cross-strata, and interdune polygons.

12
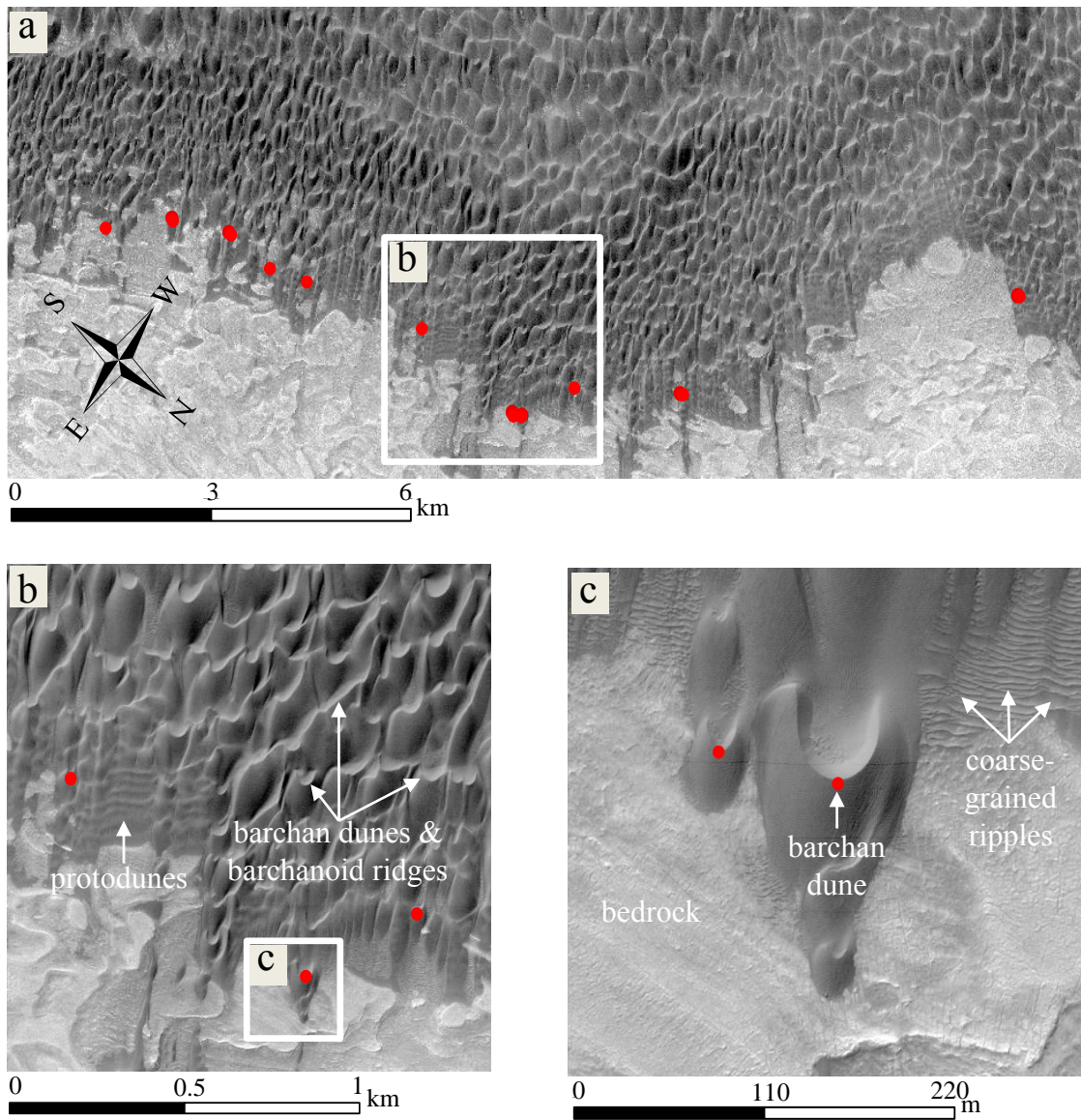
Figure 3. Study Area 2. (a) HiRISE image of Study Area 2; red points indicate location of dune crest displacement measurements. (b) Protodunes, barchan dunes and barchanoid ridges. (c) Inset image of barchan dunes, coarse-grained ripples, and bedrock, on which the dunes are migrating.

# 4. METHODOLOGY

## 4.1 Data Collection

High Resolution Science Experiment (HiRISE) satellite images and derivative digital terrain models were used in this study to assess the dune field patterns in Olympia Undae (Table 1). In Study Area 1, 3 HiRISE images (ESP_019023_2620, ESP_026737_2615, ESP_028214_2615), a stereoscopic image (ESP_027713_2615) and a DTM (DTEPC_027739_2615_027713_2615) were used to manually digitize and measure dunes, extract DTMs of dune heights, orthorectify and correlate imagery. In Study Area 2, a HiRISE image (ESP_018427_2640), stereoscopic image (ESP_036176_2640), and a DTM (DTEPC_036176_2640_035926_2640) were used to manually digitize and measure dunes, orthorectify images, and measure slip face displacement. The resolution of all images used is 0.25 meters per pixel and the resolution of the HiRISE DTMs are 1 m.

| HiRISE ID | Study Area | Data Type | Resolution (m) | Acquisition date/Ls/Mars year | Analysis Performed |
|---|---|---|---|---|---|
| ESP_019023_2620 | 1 | Raster Image | 0.25 | 08-17-2010/135°/30 | Ripple pattern identification and underlying topography extraction; COSI-Corr correlation |
| ESP_026737_2615 | 1 | Raster Image | 0.25 | 04-09-2012/95°/31 | COSI-Corr correlation |
| ESP_028214_2615 | 1 | Raster Image | 0.25 | 08-02-2012/149°/31 | COSI-Corr correlation |
| ESP_027713_2615 | 1 | Raster Image | 0.25 | 06-24-2012/31°/31 | 2-D and 3-D dune pattern tracing and measurement; COSI-Corr orthorectification; COSI-Corr correlation |
| DTEPC_027739_2615_7713_2615 | 1 | DEM | 1 | N/A | COSI-Corr orthorectification and correlation; 3-D pattern analysis |
| ESP_018427_2640 | 2 | Raster Image | 0.25 | 02-07-2010/113°/30 | Displacement measurement; COSI-Corr orthorectification |
| ESP_036176_2640 | 2 | Raster Image | 0.25 | 04-15-2014/117°/32 | 2-D and 3-D pattern tracing and measurement; displacement measurement; COSI-Corr orthorectification |
| DTEPC_036176_2640_035926_2640 | 2 | DEM | 1 | N/A | 3-D pattern analysis; COSI-Corr orthorectification |

Table 1. HiRISE images and DTMS used in this study.

## 4.2 Dune Field Pattern Analysis

Orientation, spacing, and crest length of primary dunes, secondary dunes, wind ripples, coarse-grained ripples, and dune cross-strata were measured via heads up digitization in a geographic information system (GIS) according to the methods of Ewing et al., 2006 (Figure 4). Every identified primary and secondary dune crestline in HiRISE image ESP_027713_2615 was traced at a maximum of 1:2000. Crestlines that extended outside of the image footprint were not traced and not included in the analysis.

Crestline spacing was measured orthogonally to crest orientation. Primary dune orientation was measured by placing line segments along crestlines to average the local

sinuosity and calculate azimuth. Secondary dune orientation was measured as a single line along the crestline. Primary dune width was manually measured using satellite imagery and using the DTM by measuring from the edge of the interdune to the base of the lee of the dune. Secondary dune width was measured approximately perpendicular to crestline orientation across the area of maximum curvature. For individual dune spacing, one measurement was made for primary dunes and two measurements were made and averaged for each secondary dune.

Three-dimensional parameters for individual dunes were measured along 5 transects perpendicular to the primary crestlines. A HiRISE DTM of dune heights was generated for both study areas by manually placing over 5000 points in interdune areas or on bedrock and extracting elevation to points. A DTM was generated by interpolating between these points using a tension spline with a cell size of 1, a weight of 5 and 12 points per region. The surface was then subtracted from the original DTM to create a raster of dune heights above the interdunal surface. Slope and aspect were calculated using standard ArcGIS operations and smoothed with a low pass filter to decrease the influence of anomalously high value cells.
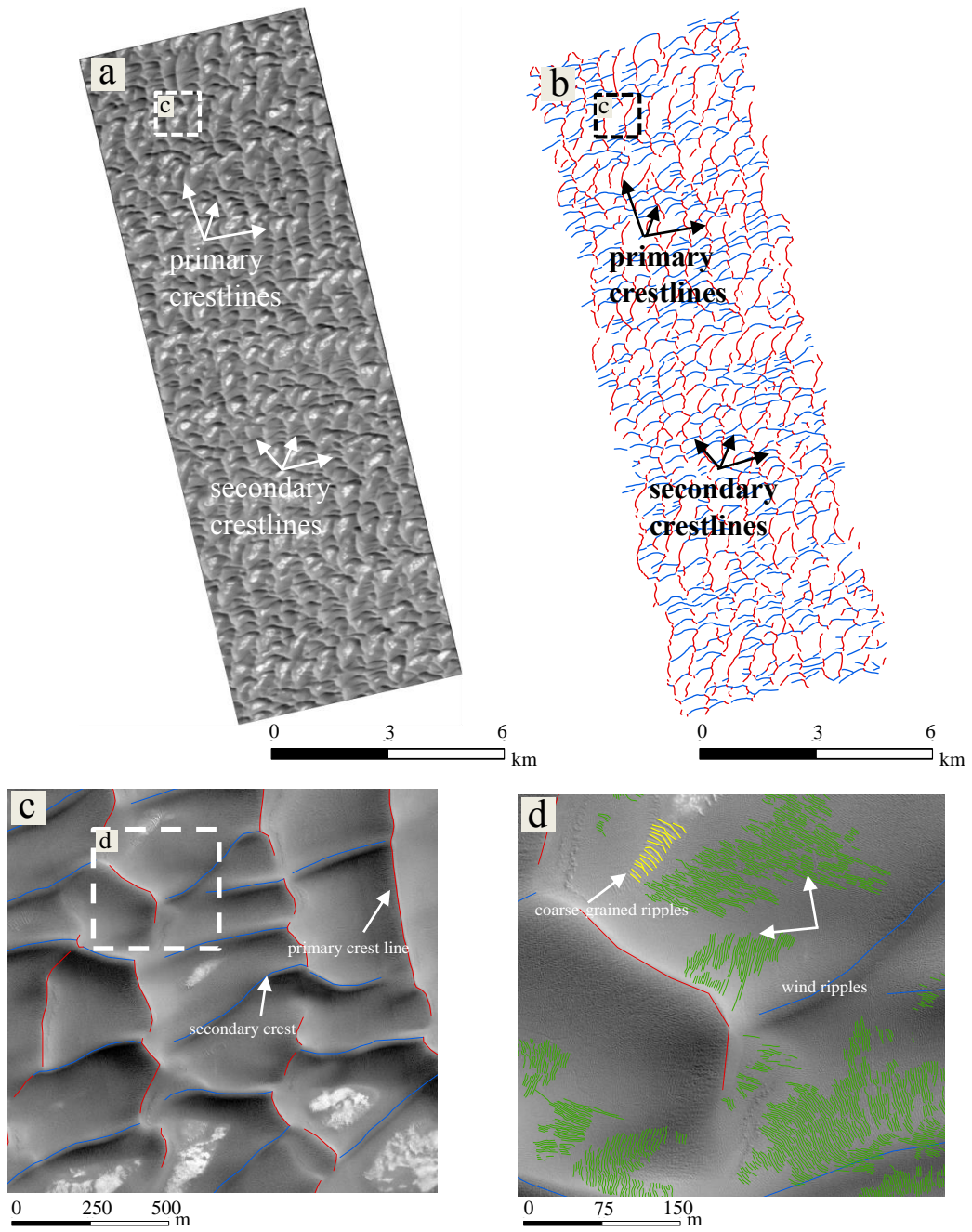
Figure 4. (a) HiRISE image of Study Area 1 showing primary and secondary dunes. (b) Dune crestline trace of primary dunes (red) and secondary dunes (blue). (c) Inset showing detail of primary and secondary dune digitization. (d) Inset of digitized coarse-grained ripples (yellow) and wind ripples (green).

17

To measure crest heights, slope heights and slope angles, dune width measurements and crest height measurements were converted to 5 meter spacing points for 34 primary dunes and 35 secondary dunes (Figure 5). 3-D parameters including dune heights, slopes and aspects were extracted and compared to 3-D parameters using regression analysis.

Wind ripple measurements were taken in a similar manner as dune measurements by manually digitizing crestlines (Figure 4). Wind ripple orientation and spacing were measured by tracing ripple trains along three transects. In each series, ripple orientation and spacing were measured and multiple measurements were made between most crestlines. Wind ripple defect density was measured by digitizing a sample of ripples between two representative primary dune crestlines. Wind ripples were digitized at a maximum of 1:300 and only traced if the crestlines were sharp, continuous and the crest trend unambiguous. Ten spatially dispersed coarse-grained ripple trains were digitized at a maximum of 1:500. Additionally, dune cross-strata were digitized at a maximum of 1:3000 and orientation measured using primary dune methodology. All orientations were measured relative to the local line of longitude.

For Study Area 2, barchan dune crestlines were traced and dune widths measured perpendicular to crestlines.
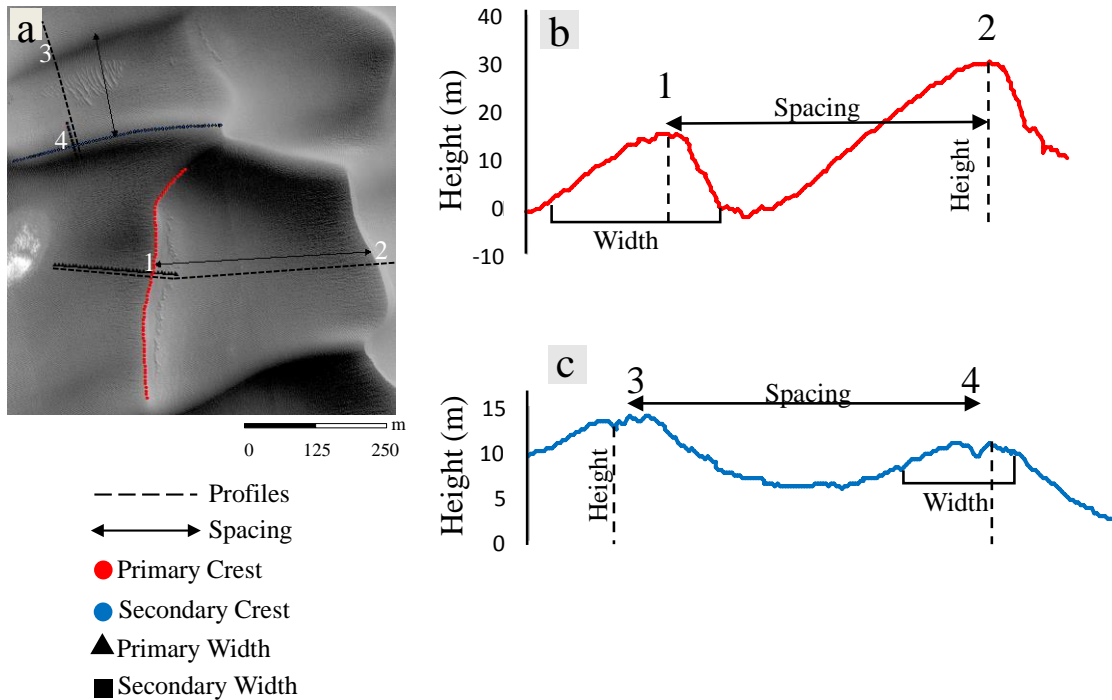
Figure 5. (a) 2-D and 3-D pattern parameters in plan view. Primary and secondary dune crests were digitized, width, and spacing were measured and crest heights and slopes were extracted. (b) Profile of primary dunes showing pattern parameters. (c) Secondary dune profile of pattern parameters.

## 4.3 COSI-Corr

Co-registration of Optically Sensed Imagery and Correlation (COSI-Corr) is a software program that measures sub-pixel ground deformation by precisely co-registering and correlating optical imagery (Leprince et al., 2007; Ayoub et al., 2009). The program is an externally developed application within an Environment for Visualizing Images (ENVI) framework. While originally designed to quantify ground deformation due to faulting and seismic events, it has been used to successfully correlate

aeolian bedforms on Earth and Mars (Vermeesch and Drake, 2009; Bridges et al., 2012; Ayoub et al., 2014). On Mars, the program uses HiRISE satellite imagery and has been able to successfully generate robust estimates of sediment fluxes based on ripple and dune displacements (Bridges et al., 2012; Ayoub et al., 2014).

Prior to using HiRISE images in COSI-Corr, the images are first processed using the planetary digital image manipulation software, Integrated Software for Imagers and spectrometers (ISIS) to remove CCD and/or jitter artifacts, resulting in radiometrically calibrated "balance cube' file composed of 9-10 red channel CCD stripes (Ayoub et al., 2014) (Figure 6). Reconstructed images, a stereoscopically derived 1 m resolution HiRISE DTMs and orthorectified images were imported into COSI-Corr for processing. All images were registered to their respective orthorectified images using at least 30 spatially distributed tie points. In Study Area 1, polygonally fractured ground and dune cross-strata were preferentially selected because these are the most stable features in the dune field. In Study Area 2, tie points were taken from bedrock at the base of the ice cap and coarse-grained ripples were selected downwind. Tie points selected on bedrock were optimized, whereas tie points selected on coarse-grained ripples in the interdune areas were not. Tie points were optimized until a good convergence was reached, typically at 5 iterations.

Residual error is comprised of DTM error and jitter/CCD error (Bridges et al., 2012; Ayoub et al., 2014). DTM error includes expected vertical precision (EVP) error and ripple and dune displacement between image acquisitions, which bias DTM extraction (Ayoub et al., 2014). DTM precision can be estimated by the following:

EVP = (Δp × IFOV) ÷ Tan (α), where Δp is the estimated pixel matching quality, IFOV is the minimum resolution of the stereographic images, and α is the parallax angle (Sutton et al., 2014). Estimated displacement bias due to DTM error for Study Area 1 is 0.219 meters which is negligible, given extrapolated maximum ripple displacements of over 4 meters. The time between stereo image acquisitions is only two days; therefore, topographic changes due to dune and ripple migration are negligible sources of error.
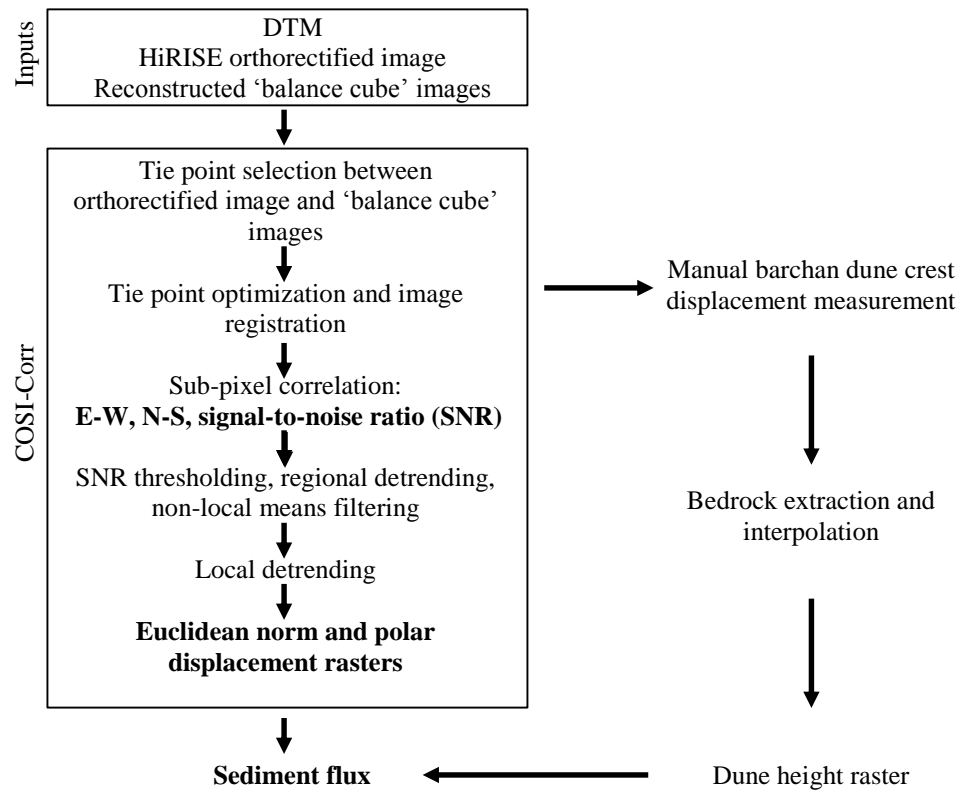


Figure 6. COSI-Corr processing chain for Study Area 1 and Study Area 2.

Jitter/CCD error is the highest magnitude error and is caused by misalignment of the CCD stripes and satellite jitter during acquisition. CCD error is modeled and corrected in ISIS and images are 'dejittered' as found necessary (Ayoub et al., 2014). In COSI-Corr, calculated misregistration error is thought to reflect satellite jitter and is on the order of centimeters for images used in this analysis (Ayoub et al., 2014). Stable ground displacement is likely caused by CCD/jitter artifacts and are reported with ripple displacements, typically on the order of 10s of centimeters. For dune displacement measurements in Study Area 2, stable ground displacements were measured adjacent to the dunes and subtracted from dune displacement.

All images were correlated using the statistic engine feature in COSI-Corr using the following parameters: 70 x 70 window, 16 step, and 15 pixel search window. The maximum observable displacement is dependent upon the search window and this parameter has a strong influence on the accuracy of the correlation result. Since individual ripple patterns are similar in appearance, a large search window may result in the miscorrelation of ripples, whereas a low search value will not capture maximum displacement (Bridges et al., 2012). To minimize this risk, a search window of 15 pixels, which corresponds to the average ripple spacing in the study area plus several pixels, was selected. The resultant product is a multi-band raster comprised of E-W displacement, N-S displacement, and signal-to-noise ratio (SNR).

Once data was generated, decorrelated pixels were removed by cleaning pixels above a minimum SNR value, determined by the amount of decorrelation occurring in each raster. Decorrelation is thought to occur at the point where ripples migrate farther

22

than the program COSI-Corr tracks (Bridges et al., 2012). To remove longer wavelength parabolic error, which may be caused by differences in the DTM spheroid and ellipsoid, the images were detrended using the following parameters: 10 decimation, 2nd degree polynomial fit, 1 iteration. The resultant raster was then filtered using a non-local means filter with the following parameters: H parameter 1.6 times the displacement of the E/W and N/S bands measured in interdunal areas,  search area of 21, and  5 x 5 patch size with averaging weighting. Residual tie point error likely includes changes in frost cover detected by COSI-Corr as displacement and non-optimized tie point error in Study Area 2.

To calculate ripple displacement for Study Area 1, rasters were detrended locally using the same parameters listed above to remove high frequency, low amplitude jitter artifacts. The displacement magnitude and polar displacement were calculated relative to the local longitude. To estimate stable ground error, displacement was measured in the interdune areas for each locally detrended area. Rasters with high error were discarded and the displacement in low error areas averaged. Sediment flux was measured using width-averaged profiles approximately perpendicular to the primary dune crestline trend. Profiles were 24 meters wide and points were placed every 4 meters at the resolution of the correlation raster and terminated at the point of dune decorrelation. Maximum displacement was calculated by averaging the last row of the trend lines of all transects.

To calculate sediment flux in Study Area 1, ripple displacements were plotted against dune height and displacement was extrapolated to the maximum dune height along each transect. Ripple topography is not resolvable using the HiRISE DTMs.  On

23

Earth, the ripple height to wavelength ratio varies between 5:1 and 15:1, but is typically 10:1. The 10:1 ratio was used to estimate ripple crest heights and multiplied by 0.5 to approximate average ripple height (Bridges et al., 2012). To calculate maximum bedload (reptation flux), ripple height was then multiplied by ripple displacement to extrapolate to the dune crest. This value was then multiplied by 1/3 to approximate the spatially averaged dune and interdune reptation (bedload) flux (Ould Ahmedou et al., 2007). The saltation to reptation ratio determined for another area of Mars by Bridges et al., 2012 is 4:1. Given that primary dune crest translation was not observed over the time studied I Study Area 1, total flux was estimated by multiplying the bedload flux by 5. Displacement in Earth years was determined by dividing the bedload flux by the number of days between acquisition and multiplying by 365. The previous operations are summarized in the following equation:

$$\text{Total sediment flux (m}^3 \text{ m}^{-1} \text{ yr}^{-1}) = \frac{\left(\text{max ripple displacement (m)} \times \left(\frac{0.1 \times \text{wavelength (m)}}{2}\right) \times \left(\frac{1}{3}\right) \times (5)\right) \times 365}{\text{Earth days}}$$

For Study Area 2, reptation + saltation flux was calculated by manually measuring the crest displacement of 10 upwind barchans dunes. Displacement error was manually measured on stable or coarse-grained rippled ground adjacent to the dune. The magnitude and orientation of erroneous stable ground displacement was subtracted from each crest displacement measurement. Dune displacement was then multiplied by max dune height and 1/3 to estimate the spatially averaged saltation + reptation flux (Ould Ahmedou et al., 2007). Total flux was then divided by the time between image

acquisitions in Earth days and multiplied by 365 to determine sediment flux per Earth year.

# 5. MEASURED DUNE AND RIPPLE PARAMETERS

*5.1 Two-Dimensional Dune Pattern Analysis*

Crestline digitization serves as a means to statistically assess the distributions of crestline length, spacing and defect density within HiRISE image ESP_027713_2615 in Olympia Undae. These parameters relate to the overall maturity of the patterns and can be used to infer the geomorphic evolution of dune fields (Werner and Kocurek, 1999; Ewing et al., 2006; Ewing et al., 2010).

The four primary parameters analyzed are defect density, spacing, crest length, and crest orientation (Ewing, et al., 2006). As the pattern moves towards steady state, defect density tends to be reduced, spacing and crest length increased and crest orientation becomes less variable (Ewing, et al., 2006). Dune spacing is considered the most representative parameter and is directly related to the length of construction time (Werner and Kocurek, 1999; Ewing, et al., 2006). There are two general types of patterns: simple patterns and complex ones. Simple patterns emerge under uniform boundary conditions. In a simple system, pattern parameters may vary spatially, if conditions across the field change. Complex patterns emerge when boundary conditions, such as sediment availability or the wind regime change. Generally, the emergence of a new pattern occurs more quickly than the time it takes for an established pattern to be reworked (Ewing, et al., 2006). The stability of a complex pattern is directly related to the defect density of the first generation dune crestlines, since crest re-orientation

propagates from defects (Ewing, et al., 2006). The orientation and spacing of the first generation of dunes in a complex system can act as a boundary condition under which the second generation of dunes evolved, limiting their maximum crest length (Ewing, et al., 2006, Ewing et al., 2010).

|  | Primary Crestlines | Secondary Crestlines | Coarse-grained Ripples (Type D) | Wind Ripples (Type A-C) |
|---|---|---|---|---|
| Crest length (m) |  |  |  |  |
| Count (n) | 741 | 724 | 811 | 804 |
| Mean | 238 | 321 | 19 | 22 |
| Median | 179 | 294 | 17 | 18 |
| Standard deviation | 199 | 172 | 10 | 19 |
| Coefficient of variation | 0.833 | 0.536 | 0.521 | 0.832 |
| Spacing (m) |  |  |  |  |
| Count (n) | 193 | 280 | 764 | 2055 |
| Mean | 464 | 285 | 6.0 | 2.2 |
| Median | 456 | 238 | 5.0 | 2.2 |
| Standard deviation | 160 | 167 | 3.7 | 0.4 |
| Coefficient of variation | 0.344 | 0.586 | 0.619 | 0.168 |
| Defect density | 0.004 | 0.003 | 0.051 | 0.045 |

Table 2. 2-D pattern parameters measured in Study Area 1 for primary dunes, secondary dunes, coarse-grained ripples, and wind ripples.

Within Study Area 1, the primary dunes are spaced at 464 m and the secondary dunes at 238 m. The primary dune spacing is less variable than secondary dunes with a coefficient of variation at 0.334 vs. 0.586 (Table 2, Figure 7). The defect density of primary dunes is 0.004 and of the secondary dunes is 0.003 (Table 2). The mean crest length of the primary dunes is 238 m with a standard deviation of 199 and the mean of the secondary crests are longer at 321 m with a standard deviation of 172 (Table 2, Figure 7). Median primary crest length is 179 m in comparison to 294 m for secondary

dunes. The primary dune crests have a coefficient of variation of 0.833 and are more variable than the secondary dunes with a coefficient of variation of 0.536 (Table 2). Primary dune circular variance is greater than secondary dunes (0.06 vs. 0.05, Figure 8). Interdune area in Study Area 1 is 9.675 million m$^2$ and is 9.18% of the total surface area.
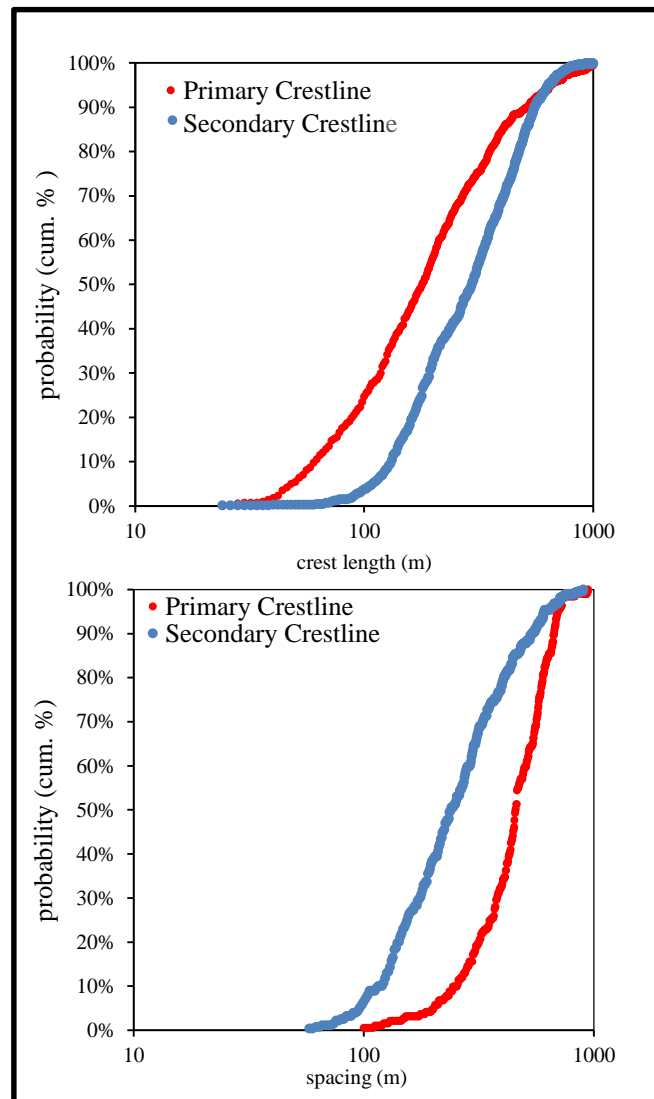


Figure 7. Primary and secondary dune cumulative probability curves for dune spacing and crest length. Secondary dunes have longer average and less variable crest lengths than primary dunes. Primary dunes are more widely and evenly spaced than secondary dunes.

28
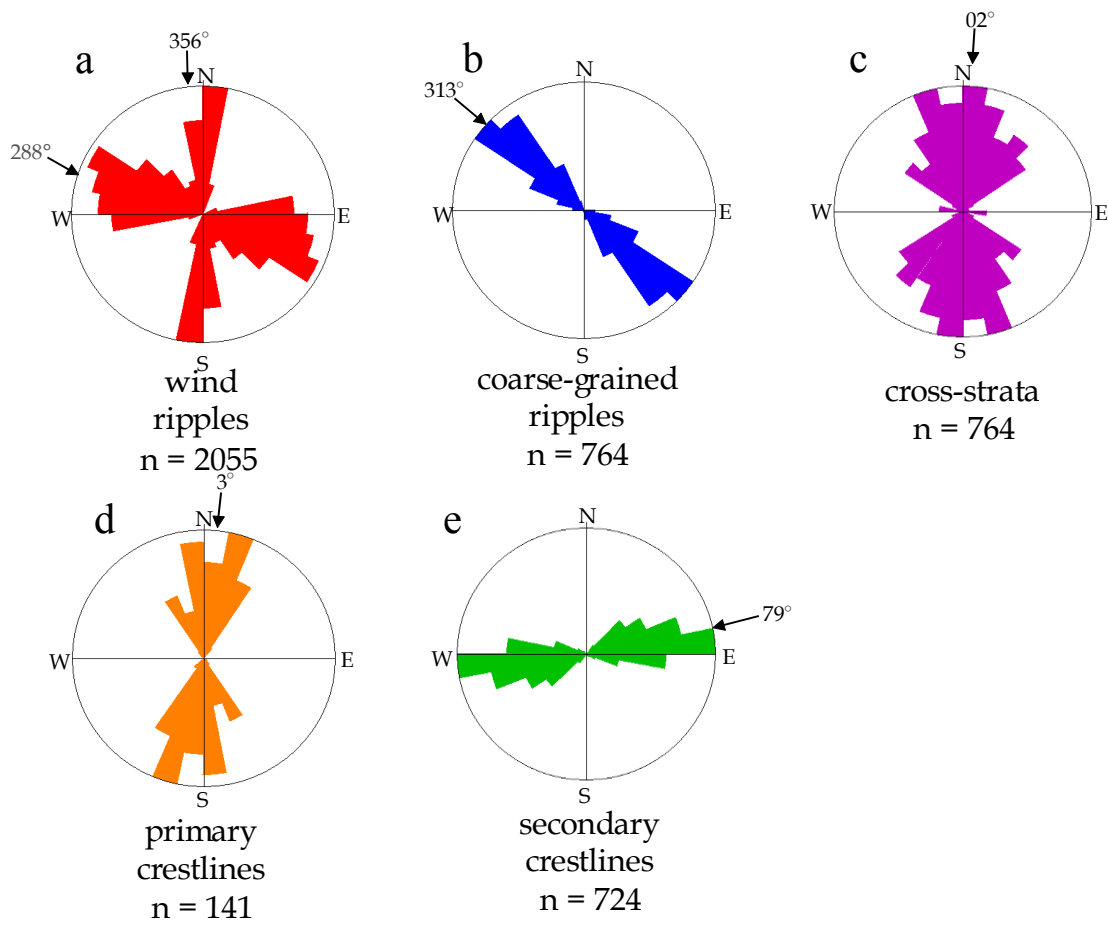
Figure 8. Rose diagrams of crestline orientations for (a) wind ripples, (b) coarse-grained ripples, (c) cross-strata, (d) primary crestlines, and (e) secondary crestlines. North is zero degrees and values increase clockwise. Mean orientation and number of measurements are included with each rose. There are two wind ripple orientation modes, N-S and SE-NW. Secondary dunes trend perpendicularly to the primary crestlines. Mean orientation of cross-strata is similar to the primary dunes.

29

| Primary Dunes | | | Secondary Dunes | |
|---|---|---|---|---|
| Crest Length (m) | | | Crest Length (m) | |
| Average | 632 | | Average | 350 |
| Minimum | 194 | | Minimum | 108 |
| Maximum | 1609 | | Maximum | 806 |
| Standard Deviation | 328 | | Standard Deviation | 135 |
| Coefficient of Variation | 0.520 | | Coefficient of Variation | 0.387 |
| | | | | |
| Spacing (m) | | | Spacing (m) | |
| Average | 470 | | Average | 312 |
| Minimum | 181 | | Minimum | 92 |
| Maximum | 712 | | Maximum | 596 |
| Standard Deviation | 143 | | Standard Deviation | 132 |
| Coefficient of Variation | 0.305 | | Coefficient of Variation | 0.424 |
| | | | | |
| Width (m) | | | Width (m) | |
| Average | 243 | | Average | 41 |
| Minimum | 144 | | Minimum | 23 |
| Maximum | 397 | | Maximum | 60 |
| Standard Deviation | 77 | | Standard Deviation | 8 |
| Coefficient of Variation | 0.318 | | Coefficient of Variation | 0.203 |
| | | | | |
| Crest Height (m) | | | Crest Height (m) | |
| Average | 26 | | Average | 24 |
| Minimum | 15 | | Minimum | 15 |
| Maximum | 37 | | Maximum | 34 |
| Standard Deviation | 5 | | Standard Deviation | 6 |
| Coefficient of Variation | 0.210 | | Coefficient of Variation | 0.226 |
| | | | | |
| Lee Height (m) | | | North Height (m) | |
| Average | 12 | | Average | 23 |
| Minimum | 2 | | Minimum | 21 |
| Maximum | 24 | | Maximum | 24 |
| Standard Deviation | 3 | | Standard Deviation | 9 |
| Coefficient of Variation | 0.302 | | Coefficient of Variation | 0.379 |
| | | | | |
| Lee Slope (°) | | | North Slope (°) | |
| Average | 16 | | Average | 15 |
| Minimum | 15 | | Minimum | 9 |
| Maximum | 35 | | Maximum | 20 |
| Standard Deviation | 3 | | Standard Deviation | 3 |
| Coefficient of Variation | 0.174 | | Coefficient of Variation | 0.209 |
| | | | | |
| Stoss Height (m) | | | South Height (m) | |
| Average | 14 | | Average | 23 |
| Minimum | 3 | | Minimum | 20 |
| Maximum | 25 | | Maximum | 25 |
| Standard Deviation | 4 | | Standard Deviation | 8 |
| Coefficient of Variation | 0.290 | | Coefficient of Variation | 0.366 |
| | | | | |
| Stoss Slope (°) | | | South Slope (°) | |
| Average | 10 | | Average | 11 |
| Minimum | 3 | | Minimum | 5 |
| Maximum | 18 | | Maximum | 18 |
| Standard Deviation | 2 | | Standard Deviation | 3 |
| Coefficient of Variation | 0.221 | | Coefficient of Variation | 0.229 |
| | | | | |
| Number of Dunes | 34 | | Number of Dunes | 35 |

Table 3. 2-D and 3-D pattern parameters measured in Study Area 1 for primary dunes and secondary dunes.

*5.2 Three-Dimensional Dune Pattern Analysis*

Analyzing dune-field patterns in three-dimensions from DEMs is a relatively new area of study and serves as a means beyond two-dimensional analysis to assess pattern development and boundary conditions of pattern evolution (Baitis et al., 2014). Topographic profiles over the primary dunes show that the dunes are asymmetric with an average stoss slope angle of 10° and lee slopes angle of 16° (Table 3). The average maximum lee slope measured from 34 number of dunes is 35° and the maximum average stoss slope of 35 number of dunes is 18°, which is within the typical range of terrestrial dunes (Baitis et al., 2014). The secondary dunes also show a degree of asymmetry with a 15° average north-facing slope and an average 11° south-facing slope (Table 3). Additionally the average maximum of both the north and south slopes is 20° and 18°, respectively, indicating that the difference between maximum slopes for secondary dunes is much less than for primary dunes. The average bedform width of primary dunes is 243 m in comparison to 41 m for secondary dunes.

The relationship between 2-D and 3-D dune parameters have been used to study the controls on the development of different dune types and to assess spatial heterogeneity in dune field patterns (Baitis et al., 2014). For this study, all correlations reported as significant have $R^2$ values greater than 0.1, analysis of variance f-values less than 0.05, and two-tailed Student t-test p-values for the dependent variable less than 0.05. In Study Area 1, primary dunes have higher correlations for more variables in comparison to secondary dunes (Figure 9). The highest correlations ($R^2$) for primary dunes are between the following: maximum stoss slope height and width (0.66), average

stoss slope height and width (0.61), maximum lee slope height and width (0.66), average lee slope height and width (0.40). Lesser correlations occur for maximum stoss slope height and spacing (0.29), average stoss slope height and spacing (0.27), average lee slope height and spacing (0.15), average dune crest height and spacing (0.24), average dune crest height and dune width (0.35), and dune width and spacing (0.17). Surprisingly, there are no significant correlations for crest length and spacing, crest length and average crest height, and stoss and lee slope heights and crest length.

For secondary dunes in Study Area 1, the significant relationships between parameters are anti-correlated. The strongest relationships are between average south slope height and width (0.22), maximum north slope height and width (0.19), and average north slope height and width (0.17) (Figure 10). All other parameter correlations are insignificant. The trend in slope for significant correlations is positive for primary dunes and negative for secondary dunes. For both dune types, 2-D and 3-D parameters do not change significantly from N-S, as measured in 5 E-W trending transects.

## 5.3 Ripple Classification

Ripple types were visually identified, classified and related to the dune topography on which these ripples occur in order to better understand the distribution of ripples occurring in Study Area 1 and the topographic controls on ripple patterns.
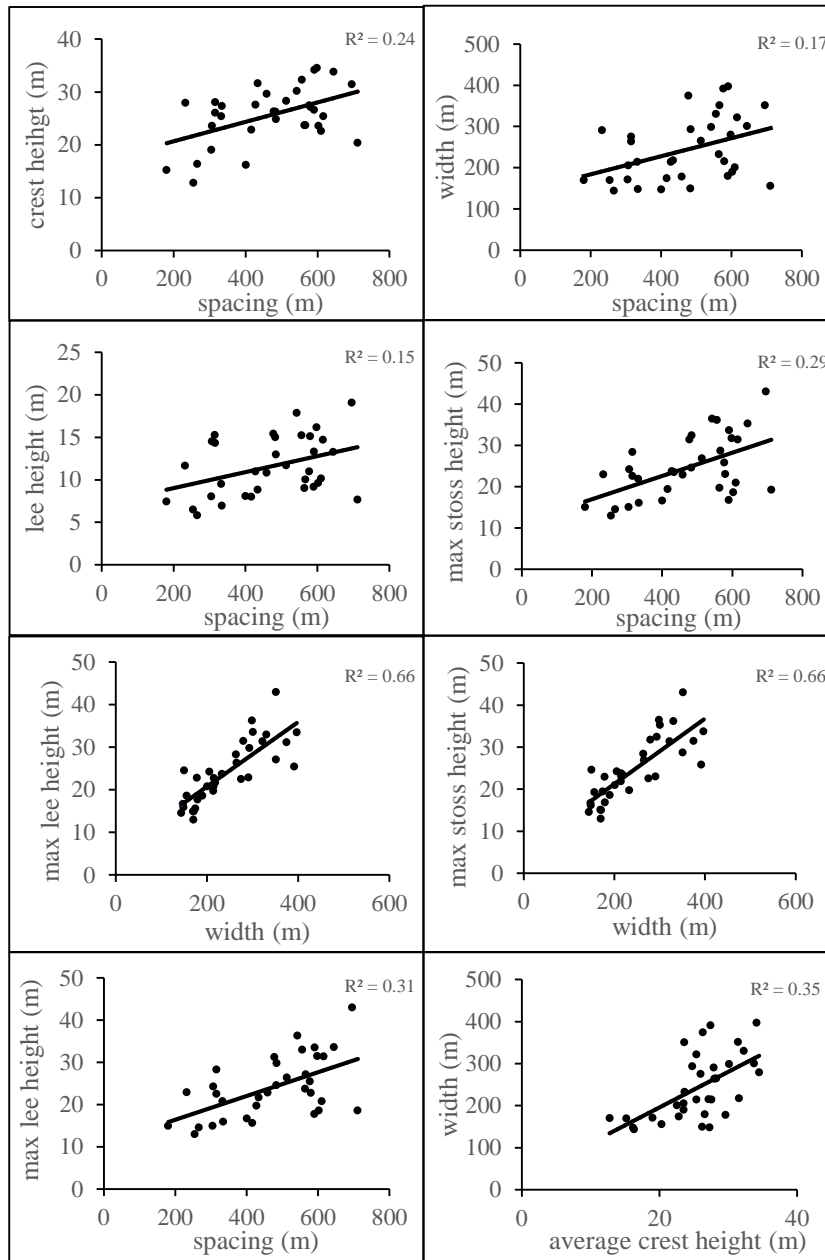
Figure 9. Examples of 2-D and 3-D pattern parameter regression analysis for primary dunes. All correlations shown have $R^2$ values greater than 0.1, Analysis of Variance (ANOVA) f-values less than 0.05, and two tailed Student's t-test p-values, less than 0.05. Primary dunes have higher correlations for more variables than secondary dunes. Similar to the results of Baitis et al., 2014's analysis of dunes at White Sands, New Mexico, primary dune show significant positive correlations between 2-D and 3-D dune parameters.
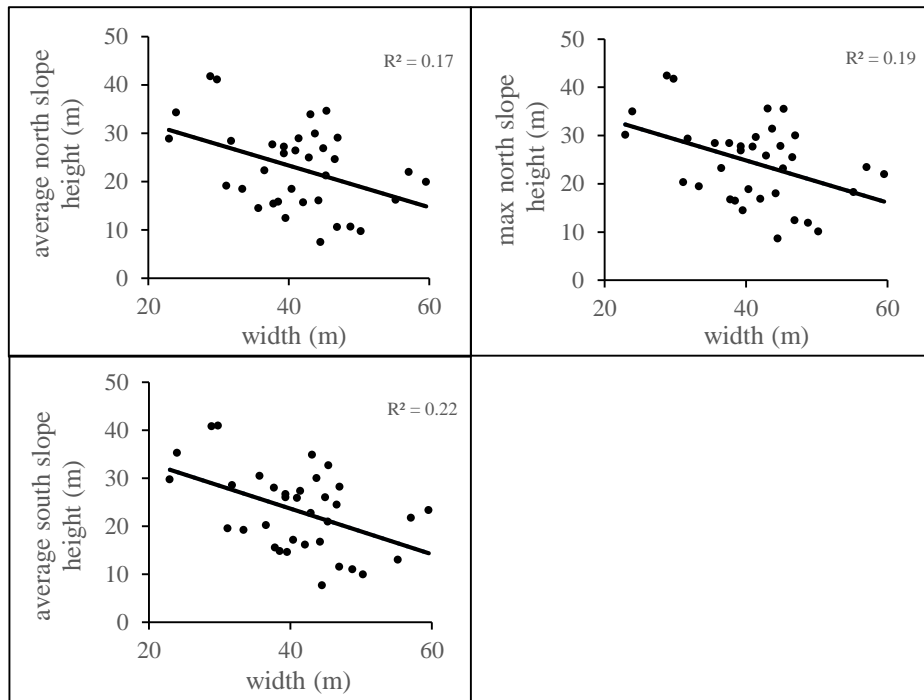
Figure 10. 2-D and 3-D pattern parameter regression analysis for secondary dunes. All correlations shown have $R^2$ values greater than 0.1, Analysis of Variance (ANOVA) f-values less than 0.05, and two tailed Student's t-test p-values, less than 0.05. Secondary dunes have only three significant correlations, which are anti-correlated.

In Study Area 1, four classes of ripples were visually identified: Type A are straight crested 2-D and sinuous 3-D wind ripples, Type B ripples are cross-hatch wind ripples with intersecting crestlines, Type C are a mottled and broken-up wind ripple pattern and Type D are long-wavelength ripples, interpreted as coarse-grained ripples (Figure 11) (Ewing, et al., 2010). Type A and C both occur at high average slopes (12°, 11°), whereas Type B and D occur at the lowest (9°, 5°) (Table 4). Type C occur at the highest average dune height (23 m), whereas Type B and D occur at the lowest (10 m, 1 m), in comparison to a local interdune area height of ~0 m. Type A ripples
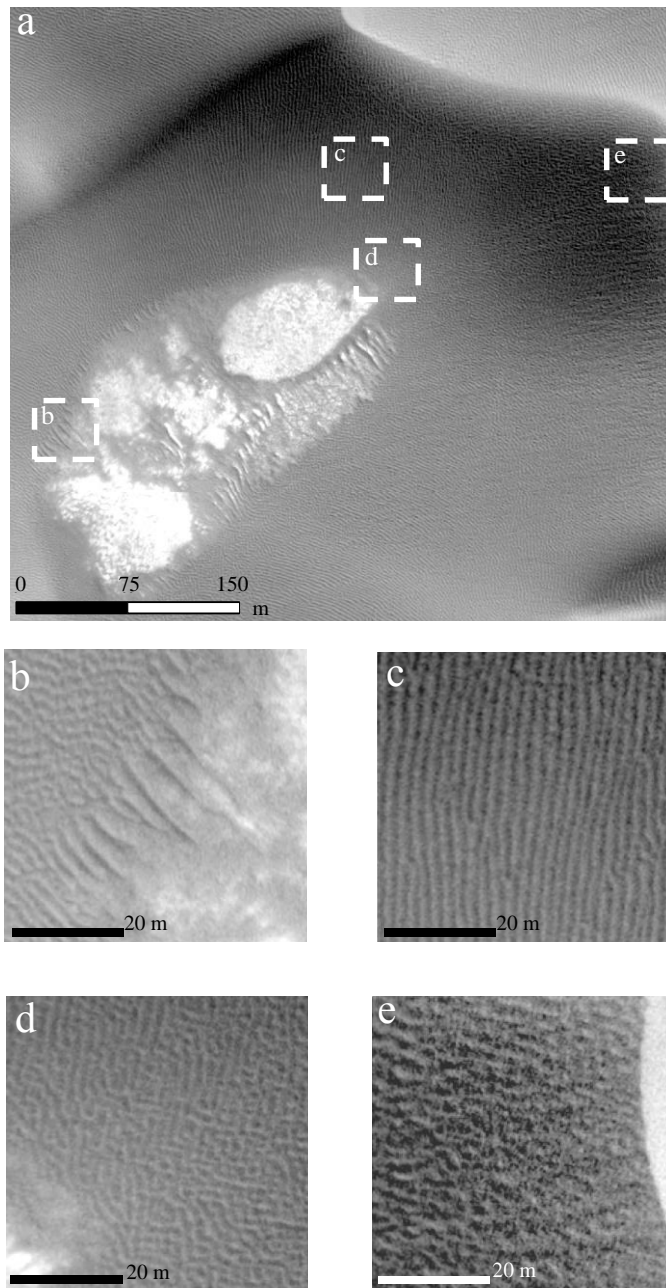
Figure 11. (a) Context image showing location of ripple types. (b) Type D ripples, which have a longer average wavelength than other ripple types and typically occur in interdune areas. (c) Type A ripples have laterally continuous crests and occur in interdune areas as well as at higher dune heights. (d) Type B ripples, which have discontinuous intersecting crests. (e) Type C ripples, which occur at high average dune heights, are a mottled and subdued discontinuous pattern.

35

occur on the dunes, but not in the periglacial polygonal areas and near the brink of the primary dunes. Type B ripples frequently occur adjacent to the interdunal polygon area, but can also occur on the dunes at higher heights. Type C frequently occur near the brink of the primary and secondary dunes and also occur in the lee of the primary dunes at lower heights. Type D occur almost exclusively in the interdune areas.

| Total points (n) | Type A | Type B | Type C | Type D |
|---|---|---|---|---|
| Height (m) | | | | |
| Mean | 13 | 10 | 23 | 1 |
| Median | 12 | 6 | 23 | 0 |
| Standard Deviation | 9 | 9 | 8 | 3 |
| Coefficient of Variation | 0.687 | 0.961 | 0.348 | 4.47 |
| | | | | |
| Slope (°) | | | | |
| Mean | 12 | 9 | 11 | 5 |
| Median | 12 | 8 | 10 | 4 |
| Standard Deviation | 5 | 4 | 7 | 3 |
| Coefficient of Variation | 0.431 | 0.473 | 0.644 | 0.600 |

Table 4. Dune topographic parameters measured for ripple-covered areas in Study Area 1.

*5.4 Ripple and Dune Migration Rates*

To assess aeolian transport under current climate conditions, ripple displacement was calculated using COSI-Corr in Study Area 1 and dune displacement was manually measured in Study Area 2 (Figure 12).

In Study Area 1, displacements were tracked in all ripple patterns both on the dunes and in the interdune areas. The average ripple displacement in the 95% of the 6 locally detrended areas is ~1.33 m yr$^{-1}$ ± 0.135 m error calculated from the displacement of the interdune areas (all "years" in this thesis are Earth years unless specifically

36

referred to as Mars years). Extrapolated to the maximum dune height along the width-averaged profiles, maximum ripple displacement is estimated to be 2.23 m. Given an average ripple wavelength of 2.24 m, using the 1:10 crest wavelength to height ratio (De Silva, 2010; Bridges et al., 2012) and assuming that mean ripple height is ½ the estimated crest height, the reptation flux at the max dune height is 0.249 $m^3$ $m^{-1}$ $yr^{-1}$ (Bridges et al., 2012). Ripple displacement increases linearly up the stoss slope of the primary dunes.

The position of primary dune crestlines does not change significantly during the time studied in Study Area 1. Therefore, total sediment flux, which is comprised of both saltation and reptation, could not be directly calculated. However, total flux can be estimated using the saltation to reptation ratio determined by Bridges et al., 2012. Given that the ratio of average dune flux to crest flux is 1:3 and a saltation to reptation ratio of 4:1, the saltation + reptation flux is ~0.42 $m^3$ $m^{-1}$ $yr^{-1}$ (Ould Ahmedou et al., 2007).
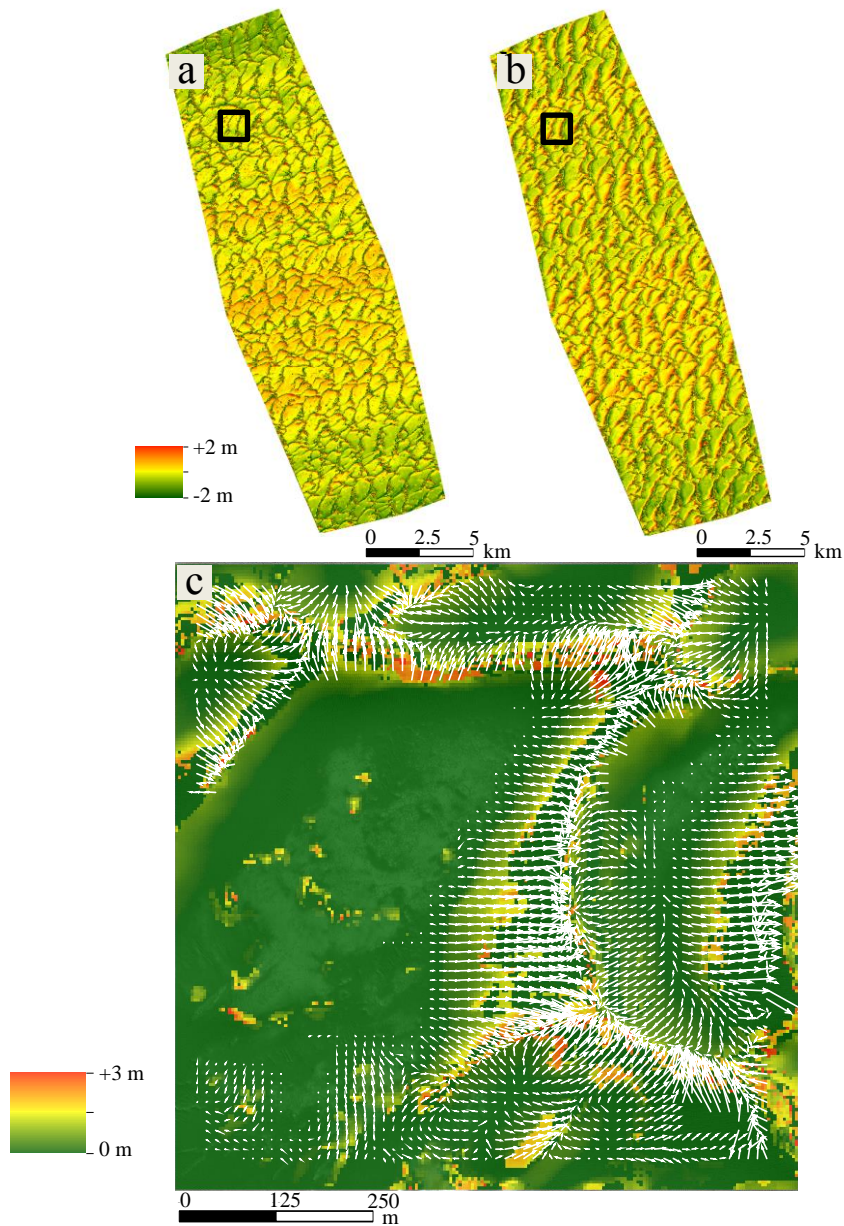
Figure 12. (a) N-S displacement raster and (b) E-W displacement raster for Study Area 1 from Mars year 30, Ls 130 to Mars year 31, Ls 135. E-W banding for both rasters is caused by satellite jitter during MRO acquisition and was removed by locally detrending areas for analysis. (c) Locally detrended magnitude displacement raster. Displacement vectors are averaged over a 15 pixel window, have a 3 pixel step and vectors within error bars, and/or in poor quality DTM areas were removed. Displacement increases up the stoss slope of the dunes, consistent with airflow speed up due to topography (Bridges et al., 2012).

38

In Study Area 2, ripple displacements could not be calculated because the ripples migrated too far during a single year. However, dune crestlines were tracked and measured to determine sediment flux. Dunes migrated an average of 1.1 m yr$^{-1}$, ranging from a maximum of 2.8 m yr$^{-1}$ and a minimum of 0.25 m yr$^{-1}$ (Figure 13). The average sediment flux based on this migration rate and the measured dune heights (average: 18 m, max: 31 m, min: 12 m) from the HiRISE DTM is ~3.5 m$^3$ m$^{-1}$ yr$^{-1}$ and the median is ~1.9 m$^3$ m$^{-1}$ yr. The average turnover time, defined as dune width divided by dune displacement, is an important in order to understand dune mobility and the residence time of sand in dunes (Warren, 2013). The average turnover time is 356 years and ranged from a minimum of 35 years to a maximum of over 1000 years.
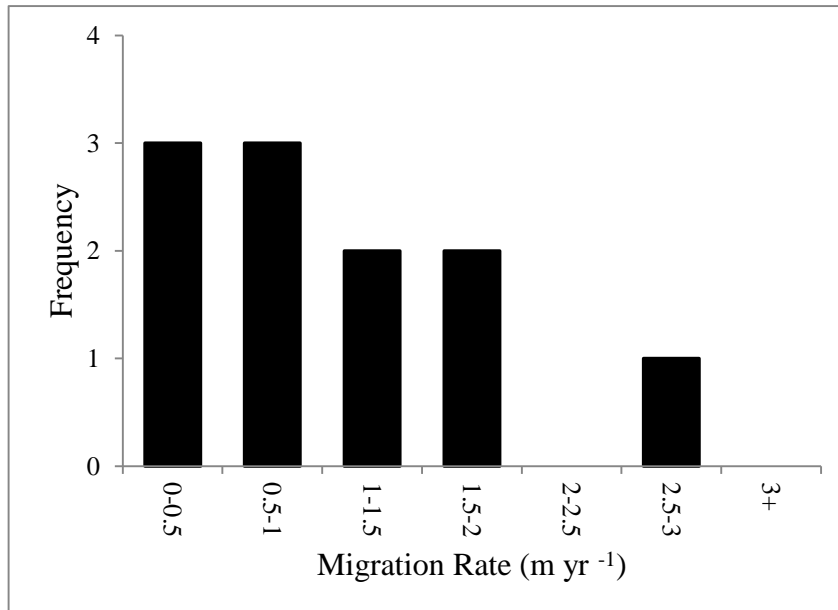


Figure 13. Histogram of dune crest displacements from Ls 113, Mars year 30 to Ls 117, Mars year 32, in Earth years for Study Area 2.

# 6. DISCUSSION

## *6.1 Two-Dimensional Dune Pattern Analysis*

Pattern analysis of Study Area 1 provides data with which to compare other areas of Olympia Undae and to determine spatial variability in the dune-field pattern in the Olympia Undae Dune Field. Recognizing the variability provides important information on how the north polar boundary conditions of Mars impact the evolution of dune field. Comparison of Study Area 1 with other areas of the dune field reveals a dune field pattern with two, nearly orthogonal crestlines that persists in most areas of Olympia Undae. This has been interpreted as a complex pattern in which younger patterns are superimposed upon older patterns and indicate a shift in wind regime or a change in sediment supply (Ewing et al., 2010). However, comparison across the field also reveals E-W spatial variation in the area of interdune areas exposed, which implies spatial changes in the sediment availability of the dune field. Changes in sediment availability have a strong control on pattern dynamics (Courrech du Pont et al., 2014) such that different orientations of patterns, such as measured in Study Area 1 and in a previous study by Ewing et al., 2010, can emerge from one wind regime. These two hypotheses are explored with the data collected in this study.

Evidence for a complex pattern includes the greater uniformity and magnitude of primary dune spacing in Study Area 1, which is most characteristic of formation time. This indicates that the primary dunes are older and more well developed than the

secondary dunes (Table 2) (Ewing et al., 2006). Additionally, the secondary dune crests form between primary dune crests, consistent with secondary dunes forming after and being constrained by primary dune topography. For all other measured parameters, the primary dune pattern is more disorganized, including shorter mean and median crest lengths, greater variability in crest orientation and greater defect density. In combination, these observations (wider primary dune spacing bounding secondary dune crests and higher primary dune disorganization for all other pattern parameters) are consistent with a pattern that is complex, with multiple generations of dune development, driven by changes in the north polar climate or sediment supply (Ewing et al., 2010).

In this interpretation, the antecedent topography of the primary dunes acts as a boundary condition to the development of the secondary dunes and explains the magnitude and uniformity of secondary crest lengths (Ewing, et al., 2010). These results are consistent with those of Ewing, et al., 2010, which measured pattern statistics for an area to the east of Study Area 1.

There are significant differences between the results of this paper and the area considered by Ewing et al., 2010. In Study Area 1, secondary dunes often do not align across primary crestlines, the defect density for both primary and secondary dunes is higher than the Ewing et al., 2010 area (0.0042 and 0.0031 vs. 0.0027 and 0.0026), and the spacing of the primary dunes is lower (464 m vs. 637 m). These results indicate that Study Area 1 is more disorganized than the Ewing et al., 2010 study area.

The Olympia Undae pattern could also be explained as the result of seasonal changes in sediment availability and interpreted as a simple pattern. In sediment

41

availability limited conditions, bedform orientation is selected for by the sediment availability limited state (Courrech du Pont et al., 2014). Sediment availability limited conditions cause dunes to be oriented in a 'fingering mode' of transport and dunes are not oriented as perpendicularly as possible to the yearly wind regime (i.e. gross bedform-normal) (Rubin and Hunter, 1987; Courrech du Pont et al., 2014).

The two conditions necessary to produce fingering mode transport, restricted sediment availability and bi-modal flow, are present in Olympia Undae (Figure 14). In this interpretation, the secondary dune orientation is controlled by the seasonally limited sediment availability conditions and extends approximately longitudinally to the flow, whereas the primary dunes crest orientation is maintained when transport is not sediment availability limited. It is possible then, that both dune types emerged and are co-evolving under relatively stable sedimentological and climatological conditions, with the divergence in bedform orientation driven by present-day climatological boundary conditions that are unique to the polar regions. However, the statistics of patterns evolving in fingering mode are not yet well understood, which makes interpretations of fingering mode from visual analysis of the pattern alone difficult to interpret. A final possible explanation for the pattern is a combination of both interpretations; the dune field pattern is the result of multiple generations of dune development under sediment availability limited conditions.

Ls 020°
09-10-2013

Ls 034°
11-24-2011

Ls 054°
01-07-2012

a

b

c

100 m

Ls 073°
02-20-2012

Ls 094°
04-09-2012

Ls 149°
08-02-2012

d

e

f

0°          90°          180°          270°

Spring          Summer          Autumnal          Winter
Equinox          Solstice          Equinox          Solstice
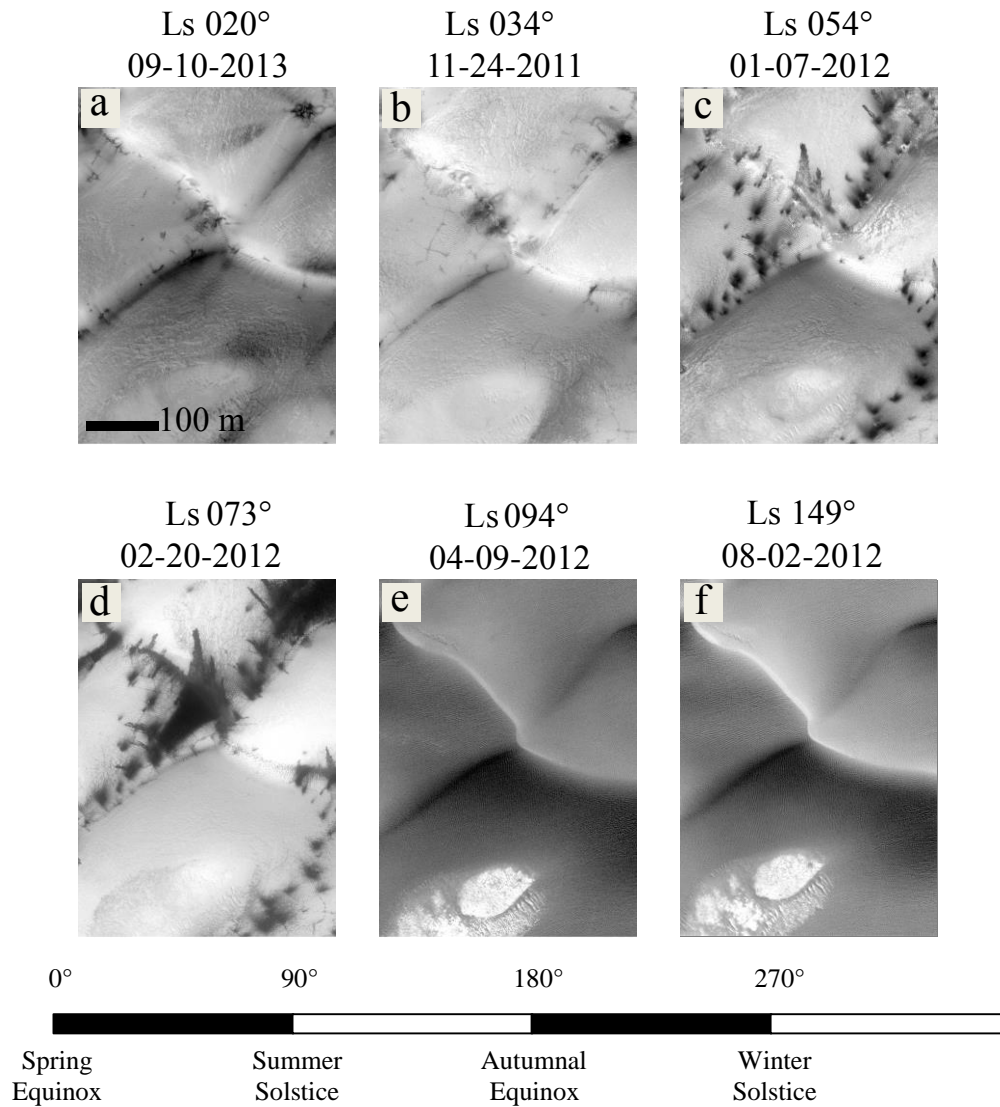
Figure 14. HiRISE images ordered by Ls in non-sequential Mars years. Dunes are covered in $CO_2$ frost for a majority of the year (Bourke et al., 2008). The black streaks seen in images a-d are likely sand avalanches (Hansen et al., 2011; Horgan and Bell, 2012). Seasonally restricted sediment availability due to frost cover (Bourke et al., 2008) may select for dune orientation and thus is a possible explanation for the well-defined reticule pattern that occurs across Olympia Undae.

ESP_036607_2785    Ewing et al., 2010    Study Area 1    ESP_036364_2620

a    b    c    d

1 km    1 km    1 km    1 km
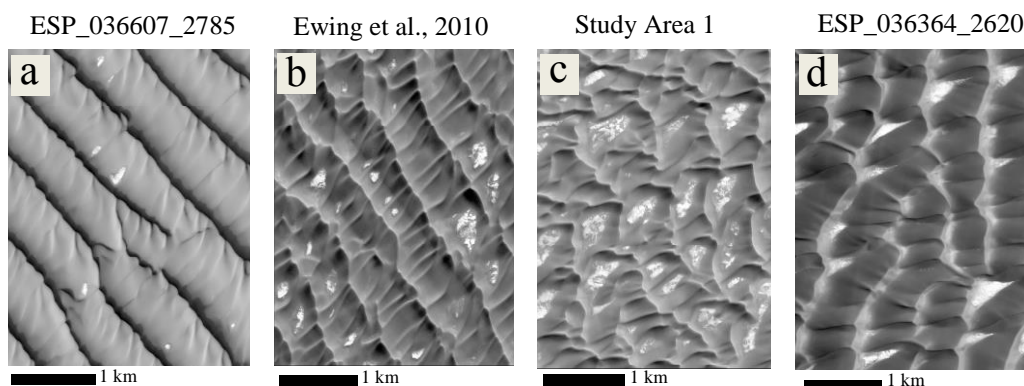
Figure 15. (a-d) Inset images of dune patterns across Olympia Undae. Images are polar stereographically projected and north is variable; see Figure 1 for image orientation. Sediment availability, as inferred by measuring interdune area is greater in (b) the Ewing et al., 2010 study area than in (c) Study Area 1. The pattern of Ewing et al., 2010 study area is more well-organized than Study Area 1. (a) ESP_036607_2785 is visibly more organized and has less interdune area than both (b) the Ewing et al., 2010 study area and (c) Study Area 1, indicating that a spatial change in sediment availability occurs between ESP_036607_2785 to Study Area 1. Pattern organization and sediment availability of (d) ESP_036364_2620 does not clearly follow the E-W trend in sediment availability and pattern organization.

Pattern statistics from Study Area 1 and the Ewing et al., 2010 study area provides an opportunity to test the hypothesis that sediment availability impacts the dune pattern. While sediment availability is difficult to quantify (Kocurek and Lancaster et al., 1999), interdune areas, which are typically absent of bedforms and are covered in frost and periglacial polygons, are an indicator of sediment availability. The Ewing et al., 2010 study area has a lower percentage of interdune area in comparison to Study Area 1 (3.88% vs. 9.18%), indicating that sediment availability is greater in Study Area 1 (Figure 15).

As mentioned previously, the Ewing et al., 2010 study area is more disorganized than Study Area 1, indicating that the pattern may be impacted by spatial variability in sediment availability. As shown in Figure 15, an area to the east of the Ewing et al.'s 2010 study area is visually better organized and contains spatially constrained interdune

areas, further supporting the hypothesis that sediment availability controls dune pattern development. Obtaining quantitative data in many more areas across the field would help better determine the relationship between sediment availability and dune pattern organization.
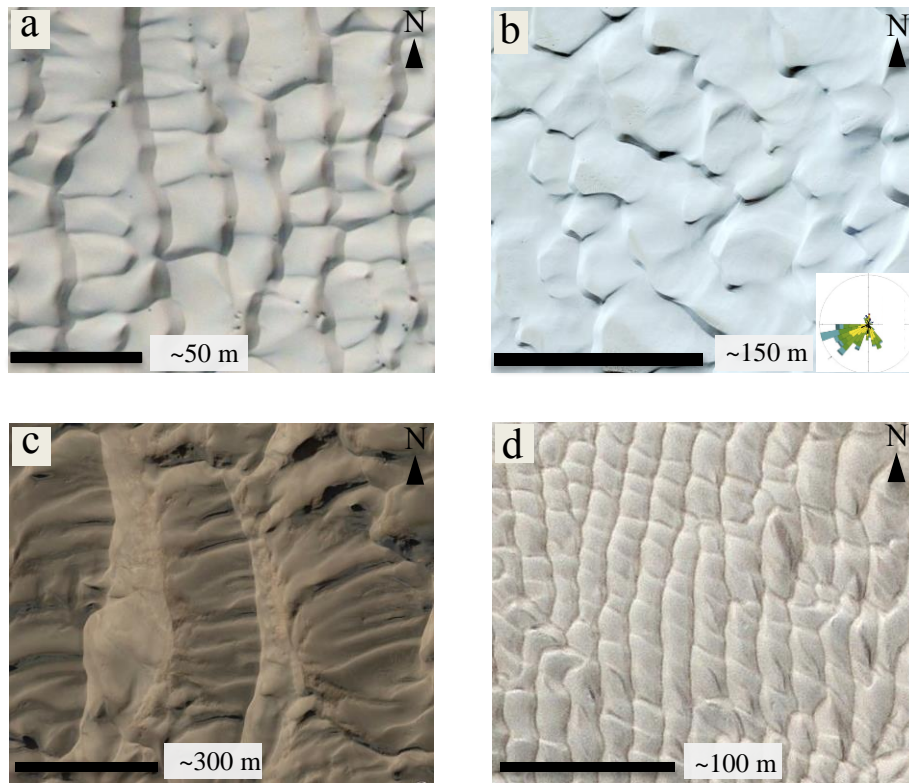


Figure 16. (a-d) Google Earth images of dune patterns in (a) the Grand Oriental Dune Field, Algeria (b), White Sands, USA (c), Great Sand Dunes, USA and (d) Taklamakan Desert, China. In each image, two distinct dune crest orientation trends are evident and the intersecting crest pattern is similar to the pattern in Olympia Undae. In (b) White Sands, the pattern is defined by two features: crescentic dunes that are approximately transverse to the yearly complex wind regime (the wind regime is represented by a rose of all wind events above critical threshold for transport from Ewing et al., 2015) and defects, which are longitudinal to gross transport direction (Ewing et al., 2015).

The dune pattern in Olympia Undae can be broadly compared to dune patterns found on Earth (Figure 16). For all dune patterns shown, there is an approximately orthogonally intersecting dune pattern, with primary dunes bounding a secondary pattern. In the northern part of the Grand Oriental dune field, there are two dune patterns that intersect approximately orthogonally: NW-SE trending dunes and SW-NE trending dunes. The NW-SE trending dunes are typically regularly spaced at 30-40 meters. In comparison, the SW-NE trending dunes are more irregularly spaced and spacing is typically between 10-40 meters. The NW-SE trending dune crestlines are more laterally continuous and the SW-NE trending dunes are bounded by the wavelength of the NW-SE trending dunes. The dunes are subordinate features and comprise larger scale draa, which are typically 300-400 meters wide.

A similar pattern occurs at White Sands, NM. There, the secondary pattern has been interpreted as longitudinally extending defects (Ewing et al., 2015) and may be analogous to secondary dune development in Olympia Undae. Future analysis of these dune patterns and their associated wind regimes on Earth could be used to better understand the evolution of dunes in Olympia Undae.

*6.2 Three-Dimensional Dune Pattern Analysis*

3-D pattern statistics indicate that the constructional process for primary dunes are different from the secondary dunes. Ewing et al., 2010 hypothesized that the secondary dunes are longitudinally constructed features where maximal deposition occurs at the intersection of the secondary dune end points and primary crestlines and

that this process is breaking up the primary pattern. The positive correlation between primary dune widths and slope heights indicates that as the bedform grew, slope angles reached a stable maximum and slope heights and dune width increased proportionately. Additionally, the primary dunes are asymmetric, with greater maximum lee slopes that are near the angle of repose and lower angled stoss slopes, consistent with asymmetric dunes forming primarily under transverse to oblique wind conditions.

In contrast, the secondary dunes show low correlations for south slope heights vs. dune width and are anti-correlated for north slope heights and dune width (Figure 9, Figure 10). This is surprising, given that all major dune types show positive correlations for significant parameters (Lancaster, 1988) and may indicate that the process for secondary dune generation is different from that of the primary dunes.

*6.3 Ripple Analysis*

Ripple types A, B, and C (wind ripples) are never superimposed on Type D (coarse-grained) ripples, indicating a common genetic process for all ripple types and supports the interpretation that the two general ripple patterns are caused by differences in grain size (Ewing, et al., 2010).

The orientation of cross-hatch Type B crestlines corresponds closely to the regional bimodal distribution of Type A ripples. Given that Type A ripple trains are caused by unidirectional secondary airflow, Type B ripples are likely caused by multi-directional winds. This is supported by the observation that Type B ripples commonly occur in areas where secondary airflow convergence is expected based on inferred wind

47

directions from Type A crest orientations. This is further supported by the observation that Type B ripples were observed to emerge from Type A ripples between Ls 94 and Ls 134.

Type C ripples, occur at the highest average heights and commonly occur near stoss slope crests where wind speed-up due to flow compression is expected. This ripple type can be explained as the terminal stage of ripple construction, where high velocity winds cause a breakup of the initial pattern. Given these interpretations, the emergence of different wind ripple patterns can be explained by a) whether the ripple formed under unidirectional or multimodal flow and b) the velocity of the secondary wind.

By comparing time series imagery of the ripple patterns, it is apparent that changes in the ripple pattern typically occur slowly. While ripple interactions, such as defect propagation were observed, no significant change in the orientation of Type A ripples were seen. At higher dune heights, more ripple activity occurs, including Type A ripples emerging from an area of Type C ripples, Type A ripples becoming more discontinuous, and Type A ripples breaking up into Type B ripples. It is possible that ripples occurring near the interdune areas are largely immobile, with only defect migration and crest maintenance occurring during the summer. The greater mobility and interactions observed at higher dune heights might be caused by stoss slope speed-up or greater sediment availability than at lower lying areas.

*6.4 Time-Series Image Analysis*

   Deposition on the lee face of dunes is controlled by the incidence angle of the wind and the dune crestline (Sweet and Kocurek, 1990). Grainfall/grainflow deposits occur between 70° and 90°, grainflow/grainfall foresets and wind ripple bottomsets deposits occur between 40° and 70°, and wind ripple deposits occur between 25° and 40° (Eastwood et al., 2012). The evolution of lee face deposits over time then, provides a record of the incident angle of the wind relative to the orientation of dune crestlines.

   There is a distinct change in the character of primary lee slopes in Study Area 1 between Mars year 30 and the three images taken during Mars Year 31 (Figure 17). In Mars year 30, the primary dunes have subdued crests and slipfaces are frequently covered in wind ripples.  In Mars year 31, primary dune crests are sharp at the peak, and slipfaces are predominantly covered in grainfall/grainflow deposits. This change suggests that an oblique wind event occurred at or before Ls 94 during Mars year 30. In comparison, no similarly oblique wind event is recorded in the Mars year 31 images, including an image taken at Ls 90. This observation supports the interpretation that the wind regime in Olympia Undae is bi-modal at least interannually and highlights strong interannual variability within the wind regime, which could be related to spatially variations in the retreat of the volatile cap and associated winds (Smith et al., 2015).


*6.5 Bedform Displacement and Sediment Flux*

   The average total sediment fluxes of upwind dunes adjacent to Planum Boreum (Study Area 2) are 7x greater than those measured in Olympia Undae (Study Area 1)

(~3.5 m$^3$ m$^{-1}$ yr$^{-1}$ and ~0.42 m$^3$ m$^{-1}$ yr$^{-1}$). Katabatic winds are density driven winds and are strongly controlled by surface slope and the confluence of katabatic flow (Parish and Bromwhich, et al., 1991). Modeled katabatic winds on Earth and Mars indicate that maximum katabatic wind velocities occur at the bottom of slopes (Smith et al., 2013). Thus, strong katabatics are expected in Study Area 2, which occurs in a low elevation area immediately adjacent to Planum Boreum. The high sediment fluxes at the upwind margin of Study Area 2 supports the occurrence of strong katabatic winds. The decrease in flux from Study Area 1 to Study Area 2 indicates that there is a spatial decay in sediment flux from the NE to the SW in the Olympia Undae, which is consistent with katabatic winds and provides further evidence that katabatic winds are the dominant transporting wind under current climate conditions.

ESP_109023_2620;
Mars year 30, Ls 135;
August 17, 2010
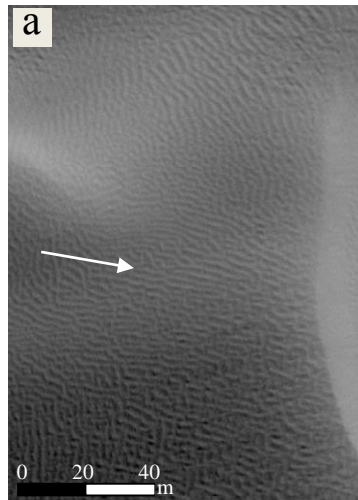
ESP_027713_2615;
Mars year 31, Ls 130;
June 34, 2012
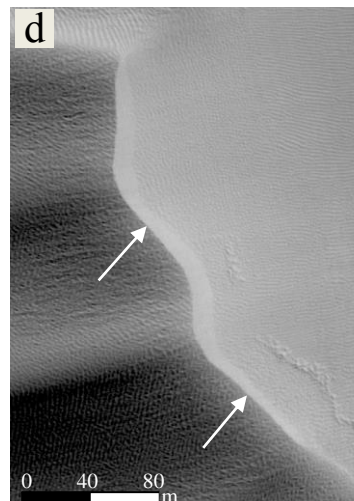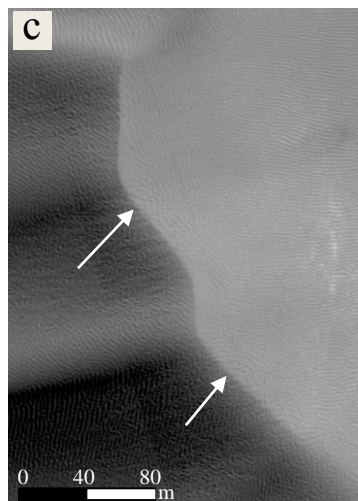
Figure 17. (a-d) Time-series of dunes in Study Area 1. (a) The ripple pattern is continuous Type A ripples at Ls 135, Mars year 30 and (c) the lee faces are frequently covered in wind ripple deposits. (b) By Ls 130, Mars year 131, (b) the ripple pattern is reworked into discontinuous Type B ripples and (d) the lee slopes are typically covered in grainfall and grainflow deposits, indicating that at least two distinct wind events occurred, one more transverse and one more perpendicular to primary crests (Eastwood et al., 2012). This indicates interannual variability in the wind regime, which may be related to spatial variability in the retreat of the volatile ice cap (Smith et al., 2015). (d) The topographically prominent textured material in the lee of the dunes in Mars year 31 may be related to mass wasting or may be uncovered interdune stratigraphy.

51

High sediment fluxes near the cap provide support for the hypothesis that the dune field is being sourced by the cavi unit and provides an important constraint on cavi erosion rates. Turnover times, defined as the time over which dunes migrate the distance of one dune width, at the upwind margin of Study Area 2, are on the order of hundreds to thousands of years. It is probable that the position of the upwind margin of the dune field is static, and thus the sediment flux rate measured in Study Area 2 must be equal to the rate of sediment supplied to the dune field. The high sediment flux measured in Study Area 2 and the spatial decay in flux to the south strongly supports the hypothesis that the cavi unit is a major source of sediment for the Olympia Undae Dune Field. Further measurements of sediment fluxes near the cap and modeling of cavi erosion should further constrain erosion and transport rates in the north polar region.

Sediment fluxes at the upwind margin of Study Area 2 are similar to the average flux measured in the equatorial dune field of Nili Patera (~3.5 $m^3$ $m^{-1}$ $yr^{-1}$ and ~2.3 $m^3$ $m^{-1}$ $yr^{-1}$) (Bridges et al., 2012). Given the seasonally sediment availability limited state of the north polar dunes, this result is surprising. The greater sediment flux in the north polar region (Study Area 2) can in part be explained because only upwind dunes were measured, whereas both upwind and down wind dunes were measured in Bridges et al., 2012. However, given that polar dunes are only mobile for approximately 30%, this alone is unlikely to fully explain the difference in magnitude of the fluxes (Bourke et al., 2008). Rephrased, it is probable that the average sediment fluxes, when sediment is available for transport (Martian summer for the polar region and year-round for the equator), are higher adjacent to the perennial ice cap than in Nili Patera.

The high sand fluxes measured in the Study Area 2 may also be related to the frequency and/or magnitude of the katabatic winds in comparison to the equatorial winds. Another possibility is that volatile defrosting decreases the friction between grains, thus increasing sediment availability in the polar regions in comparison to other areas of Mars (Hansen et al., 2011). However, this process is not yet experimentally supported and the effect of sublimation on sand grains is not well understood at the present time (Hansen et al., 2011; Horgan and Bell, 2012).

The relationship between ripple displacement and dune height provides a means of assessing the accuracy of the COSI-Corr correlation data. Ripple displacement increases linearly up the stoss slope of the primary dunes, similar to results measured in the equatorial region of Mars (Bridges et al, 2012). Given that secondary flow speed-up is expected on the stoss slope of the primary dunes, the COSI-Corr results are consistent with known the airflow dynamics of dunes on Earth (Jackson and Hunt, 1975).

*6.7 Cross-Strata*

The orientation of the dune cross-stratification provides a record of transport conditions at some point in the past. The orientation of the cross-strata is similar to the primary dunes, with both trending N-S. The variability strata orientation is greater than the primary dunes, but this can be at least partially explained by the limits on the sampling methodology, given that the strata are more discontinuous than the primary dunes and that local sinuosity thus impacts measured orientation to a greater degree than the primary dunes.

The timing of dune strata deposition is unknown, but the curvature of the ridges does not match that of the immediately downwind dunes, indicating that the cross-strata are not the deposits of these dunes. The minimum age of the strata then, is the time over which a primary dune migrates one dune wavelength. While the advance of the primary crests was below detectable levels, the turnover time of the dunes can be estimated using the dune celerity equation. Dividing average primary dune crest heights (24.4 m) by average total sediment fluxes (~0.42 $m^3 m^{-1} yr^{-1)}$, the estimated migration rate is ~0.017 m $yr^{-1}$. Given average dune widths of 243 m, the estimated turnover time for primary dunes in Study Area 1 is ~14,000 years. Similarly, the average dune spacing is 464 m and the estimated time for primary dunes to translate one wavelength is ~27,000 years. It is possible that the strata are deposits of the cavi unit and thus may be considerably older than this minimum. In either case, the similarity of the orientation of the primary dunes and the cross strata indicates that the gross climatological and sedimentological conditions of the present day north polar region are at minimum persistent over the last ~27,000 years or are recurrent.

*6.8 North Polar Sediment State*

The sediment state of a dune field is defined by sediment availability (the susceptibility of sediment to be transported), wind capacity (the potential for winds to transport sediment), and sediment supply (the source of sediment for the field) (Kocurek and Lancaster, 1999). By assessing these parameters, the sediment state of the north polar region through the Martian year can be better understood.

As previously described, sediment availability in the north polar region is directly controlled by seasonal changes in volatile frost cover (Bourke et al., 2009). Sediment supply is assumed to be the cavi unit underlying Planum Boreum (Tanaka et al., 2008). Transporting capacity is comprised of both polar easterlies and katabatic winds (Tsoar et al., 1979, Howard, 2000; Ewing et al., 2010). Given that the intensity and frequency of the katabatic winds are not well constrained, the transport capacity curve here is defined by the easterly component of the wind regime, which was modeled by Smith et al., 2015.

On Mars, the variables that control the sediment state are related. Sediment supply is inversely related to transport capacity, since aeolian processes contribute to erosion and transport of the cavi (Tanaka et al., 2008). Additionally, it is assumed here that the erosion of the cavi is inversely related to sediment availability, given that when Planum Boreum is covered in volatile frost, aeolian erosion of the cavi unit should be inhibited. Similarly, sediment availability is directly related to transport capacity; polar winds in the late spring and early summer are driven by thermal gradients due to albedo contrasts between defrosted ground and the volatile frost and the maximum early summer wind speed corresponds to peak defrosting (Smith et al., 2015).
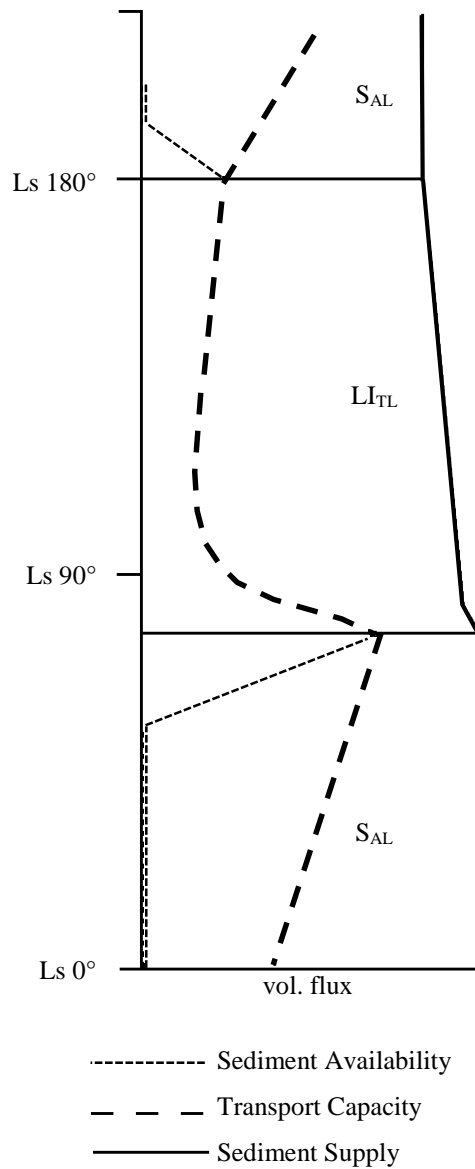
Figure 18. Sediment state diagram for the north polar region following Kocurek and Lancaster, 1999.

As shown in Figure 18, for the first part of the summer, sediment is stored in an availability-limited state. Once the downwind margin of the field first fully defrosts,

sediment availability increases until the upwind dunes are defrosted. At this point, sediment is fully available for transport and the dune field is in a transport limited lagged influx state. There is an increase in cavi erosion, but transport capacity rapidly decreases, and erosion of the cavi (decrease in sediment supply) and sediment transport is limited by the decreased transport capacity. During the late summer and early fall, volatiles begin are re-deposited. Once the upwind margin of the dune field is frosted, sediment availability decreases and sediment is stored again in an availability-limited state until the following spring/summer.

*6.9 Multi-Spatial Boundary Conditions*

The three scales of bedforms described here (ripples, dunes, dune field) reflect different time scales of formation and operate under scale dependent boundary conditions (Ewing et al., 2015) (Figure 4). The transport time scale for bedforms is positively related to the spatial scale of bedforms, such that each bedform type represents overlapping ranges of transport time scales (Ewing et al., 2015). At the smallest scale (ripples), formation time increases with ripple size and coarseness and ranges from the most recent transport event, to annual cycles (Ewing et al., 2015). At the largest scale (dune field), formation time increases with dune field size, ranging from decadal to orbital scales (Ewing et al., 2015).

The interaction of bedforms across scales controls the morphometry and pattern for all bedform types. Ripples superimposed on dunes are controlled by secondary airflow, which is slaved to the larger scale dunes (Werner, 1995; Frank and Kocurek,

1996b; Kocurek and Ewing, 2012). Grain sorting and ripple displacement are related to secondary airflow velocity, which is controlled by airflow speed up on the stoss slope of the primary dune and downwind flow separation on the leeside of the dune (Frank and Kocurek, 1996a; Frank and Kocurek, 1996b). Ripple orientation on the dune is controlled by secondary airflow deflected on the slope of the dune (Kocurek et al., 2007). On Mars, the orientation of ripples in relation to dune crestlines has been used to infer secondary flow on both primary dunes and secondary dunes (Ewing et al., 2010).

Interaction between dunes is controlled by field-scale boundary conditions and these interactions define the field-scale pattern. The boundary condition of primary dune topography may weaken spatially as a function of sediment availability, decreasing the number of dynamical variables under which secondary dunes develop, which is manifested at the field scale as greater pattern disorganization while the pattern is being reworked.

In Study Area 1, the emergence of a larger scale pattern is observed. The interdune areas are commonly in alignment from E-W. This pattern may be controlled by the effect of the sediment availability limited interdune surface on the dunes, impacting dune-dune interactions. Variability in the pattern may be an additional indicator of pattern organization and the effect of spatial variability in sediment availability on the dune pattern.

# 7. CONCLUSIONS

Boundary conditions in the north polar region of Mars constrain dune pattern development and control the magnitude of sediment fluxes. The dune pattern in Olympia Undae can be interpreted as either complex, with multiple generations of dune development, or simple, emerging due to seasonally limited sediment availability. The dune pattern varies spatially and may be related to changes in sediment availability. Three dimensional pattern analysis supports the interpretation that the primary dunes emerged under transverse to oblique wind conditions, whereas the process for secondary dune generation is not well understood. Different wind ripple types occur in Olympia Undae and are controlled by the boundary condition of the dunes. Sediment fluxes at the upwind margin of dunes adjacent to Planum Boreum are 7x higher than in Olympia Undae, supporting the interpretation that katabatic winds are the dominant transporting wind under current climate conditions.

REFERENCES

Appéré, T., Schmitt, B., Langevin, Y., Douté, S., Pommerol, A., Forget, F., … Bibring, J.-P. (2011). Winter and spring evolution of northern seasonal deposits on Mars from OMEGA on Mars Express. *Journal of Geophysical Research*, *116*(E5), E05001. http://doi.org/10.1029/2010JE003762

Ayoub, F., Leprince, S., & Avouac, J.-P. (2009). Co-registration and correlation of aerial photographs for ground deformation measurements. *ISPRS Journal of Photogrammetry and Remote Sensing*, *64*(6), 551–560. http://doi.org/10.1016/j.isprsjprs.2009.03.005

Ayoub, F., Avouac, J.-P., Newman, C. E., Richardson, M. I., Lucas, A., Leprince, S., & Bridges, N. T. (2014). Threshold for sand mobility on Mars calibrated from seasonal variations of sand flux. *Nature Communications*, *5*, 5096. http://doi.org/10.1038/ncomms6096

Bagnold, R. A. (1941). The physics of wind blown sand and desert dunes. *Methuen, London*, *265*(10).

Baitis, E., Kocurek, G., Smith, V., Mohrig, D., Ewing, R. C., & Peyret, A.-P. B. (2014). Definition and origin of the dune-field pattern at White Sands, New Mexico. *Aeolian Research*, *15*, 269–287. http://doi.org/10.1016/j.aeolia.2014.06.004

Bourke, M. C., Edgett, K. S., & Cantor, B. A. (2008). *Recent aeolian dune change on Mars*. *Geomorphology* (Vol. 94).

Bridges, N. T., Ayoub, F., Avouac, J.-P., Leprince, S., Lucas, A., & Mattson, S. (2012). Earth-like sand fluxes on Mars. *Nature*, *485*(7398), 339–42. http://doi.org/10.1038/nature11022

Calvin, W.M., James, P.B., & Hansen, C.J. (2012). Seasonal variation in volatile ices in the north polar region of Mars. *Proc. Lunar Planet. Sci. Conf. 43$^{rd}$*, Abstract 2278.

Courrech du Pont, S., Narteau, C., & Gao, X. (2014). Two modes for dune orientation. *Geology*, *42*(9), 743–746. http://doi.org/10.1130/G35657.1

De Silva, S. (2010), Comment on the largest wind ripples on Earth. *Geology*, *38*, e218, doi:10.1130/G30780C.1

Eastwood, E. N., Kocurek, G., Mohrig, D., & Swanson, T. (2012). Methodology for reconstructing wind direction, wind speed and duration of wind events from aeolian cross-strata. *Journal of Geophysical Research*, *117*(F3), F03035. http://doi.org/10.1029/2012JF002368

Ewing, R. C., Kocurek, G., & Lake, L. W. (2006). Pattern analysis of dune-field parameters. *Earth Surface Processes and Landforms*, *31*(9), 1176–1191. http://doi.org/10.1002/esp.1312

Ewing, R. C., & Kocurek, G. (2010). Aeolian dune-field pattern boundary conditions. *Geomorphology*, *114*(3), 175–187. http://doi.org/10.1016/j.geomorph.2009.06.015

Ewing, R. C., Peyret, A. B., Kocurek, G., & Bourke, M. (2010). Dune field pattern formation and recent transporting winds in the Olympia Undae Dune Field, north polar region of Mars. *Journal of Geophysical Research: Planets (1991–2012)*, *115*(E8). http://doi.org/10.1029/2009JE003526

Ewing, R. C., McDonald, G. D., & Hayes, A. G. (2015). Multi-spatial analysis of aeolian dune-field patterns. *Geomorphology*, *240*, 44–53. http://doi.org/10.1016/j.geomorph.2014.11.023

Feldman, W. C., Bourke, M. C., Elphic, R. C., Maurice, S., Bandfield, J., Prettyman, T. H., … Lawrence, D. J. (2008). Hydrogen content of sand dunes within Olympia Undae. *Icarus*, *196*(2), 422–432. http://doi.org/http://dx.doi.org/10.1016/j.icarus.2007.08.044

Fishbaugh, K. E., Poulet, F., Chevrier, V., Langevin, Y., & Bibring, J.-P. (2007). On the origin of gypsum in the Mars north polar region. *Journal of Geophysical Research*, *112*(E7), E07002. http://doi.org/10.1029/2006JE002862

Frank, A. J., & Kocurek, G. (1996). Toward a model for airflow on the lee side of aeolian dunes. *Sedimentology*, *43*(3), 451–458. http://doi.org/10.1046/j.1365-3091.1996.d01-20.x

Frank, A. J., & Kocurek, G. (1996). Airflow up the stoss slope of sand dunes: limitations of current understanding. *Geomorphology*, *17*(1-3), 47–54. http://doi.org/10.1016/0169-555X(95)00094-L

Hansen, C. J., Bourke, M., Bridges, N. T., Byrne, S., Colon, C., Diniega, S., … Thomas, N. (2011). Seasonal erosion and restoration of Mars' northern polar dunes. *Science (New York, N.Y.)*, *331*(6017), 575–8. http://doi.org/10.1126/science.1197636

61

Hayward, R. K., Mullins, K. F., Fenton, L. K., Hare, T. M., Titus, T. N., Bourke, M. C.,
… Christensen, P. R. (2007). Mars Global Digital Dune Database and initial
science results. *Journal of Geophysical Research*, *112*(E11), E11007.
http://doi.org/10.1029/2007JE002943

Horgan, B. H. N., & Bell, J. F. (2012). Seasonally active slipface avalanches in the north
polar sand sea of Mars: Evidence for a wind-related origin. *Geophysical Research
Letters*, *39*(9). http://doi.org/10.1029/2012GL051329

Howard, A. D. (2000). The role of eolian processes in forming surface features of the
Martian Polar Layered Deposits. *Icarus*, *144*(2), 267–288.

Jackson, P. S., & Hunt, J. C. R. (1975). Turbulent wind flow over a low hill. *Quarterly
Journal of the Royal Meteorological Society*, *101*(430), 929–955.
http://doi.org/10.1002/qj.49710143015

Kelly, N. J., Boynton, W. V., Kerry, K., Hamara, D., Janes, D., Reedy, R. C., …
Haberle, R. M. (2006). Seasonal polar carbon dioxide frost on Mars: CO2 mass and
columnar thickness distribution. *Journal of Geophysical Research*, *112*(E3),
E03S07. http://doi.org/10.1029/2006JE002678

Kocurek, G., & Lancaster, N. (1999). Aeolian system sediment state: theory and Mojave
Desert Kelso dune field example. *Sedimentology*, *46*(3), 505–515.
http://doi.org/10.1046/j.1365-3091.1999.00227.x

Kocurek, G., Carr, M., Ewing, R., Havholm, K. G., Nagar, Y. C., & Singhvi, A. K.
(2007). White Sands Dune Field, New Mexico: Age, dune dynamics and recent
accumulations. *Sedimentary Geology*, *197*(3), 313–331.

Kocurek, G., Ewing, R. C., & Mohrig, D. (2010). How do bedform patterns arise? New
views on the role of bedform interactions within a set of boundary conditions. *Earth
Surface Processes and Landforms*, *35*(1), 51–63. http://doi.org/10.1002/esp.1913

Kocurek, G., & Ewing, R. C. (2012). Source-to-sink: an Earth/Mars comparison of
boundary conditions for eolian dune systems. *Sedimentary Geology of Mars. SEPM
Special Publication,* (102).

Lancaster, N. (1988). Controls of eolian dune size and spacing. *Geology*, *16*(11), 972–
975. http://doi.org/10.1130/0091-7613(1988)016

Langevin, Y., Poulet, F., Bibring, J.-P., & Gondet, B. (2005). Sulfates in the north polar
region of Mars detected by OMEGA/Mars Express. *Science (New York, N.Y.)*,
*307*(5715), 1584–6. http://doi.org/10.1126/science.1109091

Leprince, S., Barbot, S., Ayoub, F. & Avouac, J. P. (2007). Automatic and precise orthorectification, coregistration, and subpixel correlation of satellite images, application to ground deformation measurements. *IEEE Trans. Geosci. Rem. Sens. 45*, 1529–1558.

Massé, M., Bourgeois, O., Le Mouélic, S., Verpoorter, C., Spiga, A., & Le Deit, L. (2012). Wide distribution and glacial origin of polar gypsum on Mars. *Earth and Planetary Science Letters*, *317-318*, 44–55. http://doi.org/10.1016/j.epsl.2011.11.035

Ould Ahmedou, D., Ould Mahfoudh, A., Dupont, P., Ould El Moctar, A., Valance, A., & Rasmussen, K. R. (2007). Barchan dune mobility in Mauritania related to dune and interdune sand fluxes. *Journal of Geophysical Research*, *112*(F2), F02016. http://doi.org/10.1029/2006JF000500

Parish, T.R., Bromwich, D. H. (1991). Continental-scale simulation of the Antarctic katabatic wind regime. *Journal of Climate*, *4*(2), 135-146.

Rubin, D. M., & Hunter, R. E. (1987). Bedform alignment in directionally varying flows. *Science (New York, N.Y.)*, *237*(4812), 276–8. http://doi.org/10.1126/science.237.4812.276

Seppälä, M., & Lindé, K. (1978). Wind tunnel studies of ripple formation. *Geografiska Annaler. Series A, Physical Geography*, *60*(1/2), 29–42. http://doi.org/10.2307/520963

Smith, D. E., Zuber, M. T., & Neumann, G. A. (2001). Seasonal variations of snow depth on Mars. *Science (New York, N.Y.)*, *294*(5549), 2141–6. http://doi.org/10.1126/science.1066556

Smith, I. B., & Holt, J. W. (2010). Onset and migration of spiral troughs on Mars revealed by orbital radar. *Nature*, *465*(7297), 450–3. http://doi.org/10.1038/nature09049

Smith, I. B., Holt, J. W., Spiga, A., Howard, A. D., & Parker, G. (2013). The spiral troughs of Mars as cyclic steps. *Journal of Geophysical Research: Planets*, *118*(9), 1835-1857. http://doi.org/10.1002/jgre.20142

Smith, Isaac B., Spiga, Aymeric, Tyler, Daniel, Ewing, R. C. (2015). Wind at the North Pole of Mars: Comparisons of Modeling and Observations. *LPI Dunes Workshop,* Abstract 8013.

Spiga, A., & Forget, F. (2009). A new model to simulate the Martian mesoscale and microscale atmospheric circulation: Validation and first results. *Journal of Geophysical Research*, *114*(E2), E02009. http://doi.org/10.1029/2008JE003242

Sutton, S., Chojnacki, M., Kilgallon, A., & HiRISE Team. (2015). Precision and accuracy of simultaneously collected HiRISE digital terrain models. *Proc. Lunar Planet. Sci. Conf. 46<sup>th</sup>*, Abstract 3010.

Sweet, M. L., & Kocurek, G. (1990). An empirical model of aeolian dune lee-face airflow. *Sedimentology*, *37*(6), 1023–1038. http://doi.org/10.1111/j.1365-3091.1990.tb01843.x

Tanaka, K. L, and R. K. Hayward (2008). Mars' north circumpolar dunes: Distribution, sources, and migration history. *LPI Dunes Workshop,* Abstract 7012.

Tanaka, K., Rodriguez, J., Skinner, Jr., J., Bourke, M., Fortezzo, C., Herkenhoff, K., … Okubo, C. (2008). North polar region of Mars: Advances in stratigraphy, structure, and erosional modification. *Icarus*, *196*(2), 318–358. http://doi.org/10.1016/j.icarus.2008.01.021

Titus, T. N. (2005). Mars polar cap edges tracked over 3 full Mars years. *Proc. Lunar Planet. Sci. Conf. 36th*, Abstract 1993.

Tsoar, H., Greeley, R., & Peterfreund, A. R. (1979). Mars: The North Polar Sand Sea and related wind patterns. *Journal of Geophysical Research: Solid Earth (1978–2012)*, *84*(B14), 8167–8180. http://doi.org/10.1029/JB084iB14p08167

Tsoar, H. (1983). Dynamic processes acting on a longitudinal (seif) sand dune. *Sedimentology*, *30*(4), 567–578. http://doi.org/10.1111/j.1365-3091.1983.tb00694.x

Vermeesch, P., & Drake, N. (2008). Remotely sensed dune celerity and sand flux measurements of the world's fastest barchans (Bodélé, Chad). *Geophysical Research Letters*, *35*(24), L24404. http://doi.org/10.1029/2008GL035921

Warren, A. (2013). *Dunes: Dynamics, Morphology*, History. John Wiley & Sons.

Werner, B. (1995). Eolian dunes: Computer simulations and attractor interpretation. *Geology*, *23*, 1107–1110.

Werner, B. T., & Kocurek, G. (1999). Bedform spacing from defect dynamics. *Geology*, *27*(8), 727–730. http://doi.org/10.1130/0091-7613(1999)027

Werner, B. T. (1999). Complexity in natural landform patterns. *Science*, *284*(5411), 102–104. http://doi.org/10.1126/science.284.5411.102

Zimbelman, J. R., Bourke, M. C., & Lorenz, R. D. (2013). Recent developments in planetary Aeolian studies and their terrestrial analogs. *Aeolian Research, 11*, 109–126. http://doi.org/10.1016/j.aeolia.2013.04.004